#### **OPEN ACCESS**



# The Early Light Curve of the Type Ia Supernova 2021hpr in NGC 3147: Progenitor Constraints with the Companion Interaction Model

Gu Lim<sup>1,2,3</sup>, Myungshin Im<sup>1,2</sup>, Gregory S. H. Paek<sup>1,2</sup>, Sung-Chul Yoon<sup>1,2</sup>, Changsu Choi<sup>1,2,4</sup>, Sophia Kim<sup>1,2</sup>, J. Craig Wheeler<sup>5</sup>, Benjamin P. Thomas<sup>5</sup>, Jozsef Vinkó<sup>5,6,7,8</sup>, Dohyeong Kim<sup>3</sup>, Jinguk Seo<sup>1,2</sup>, Wonseok Kang<sup>9</sup>, Taewoo Kim<sup>9</sup>, Hyun-Il Sung<sup>4</sup>, Yonggi Kim<sup>10</sup>, Joh-Na Yoon<sup>10</sup>, Haeun Kim<sup>10</sup>, Jeongmook Kim<sup>10</sup>, Hana Bae<sup>10</sup>, Shuhrat Ehgamberdiev<sup>11,12</sup>, Otabek Burhonov<sup>11</sup>, and Davron Mirzaqulov<sup>11</sup>, SNU Astronomy Research Center, Seoul National University, 1 Gwanak-ro, Gwanak-gu, Seoul 08826, Republic of Korea; myungshin.im@gmail.com<sup>2</sup> Astronomy Program, Department of Physics and Astronomy, Seoul National University, Gwanak-gu, Seoul 08826, Republic of Korea Department of Earth Sciences, Pusan National University, Busan 46241, Republic of Korea Korea Astronomy and Space Science Institute, 776 Daedeokdae-ro, Yuseong-gu, Daejeon 34055, Republic of Korea Department of Astronomy, University of Texas at Austin, Austin, TX, USA

Korea Astronomy and Space Science Institute of Physics, Pázmány Péter sétány 1/A, Budapest 1121, Hungary

ELTE Eötvös Loránd University, Institute of Physics, Pázmány Péter sétány 1/A, Budapest 1117 Hungary

National Youth Space Center, Goheung, Jeollanam-do 59567, Republic of Korea

Chungbuk National University Observatory, 361-763 Cheongju, Republic of Korea

Ulugh Beg Astronomical Institute, Uzbek Academy of Sciences, 33 Astronomical Street, Tashkent 700052, Uzbekistan

Received 2022 October 4; revised 2023 February 24; accepted 2023 February 27; published 2023 May 24

#### **Abstract**

The progenitor system of Type Ia supernovae (SNe Ia) is expected to be a close binary system consisting of a carbon/oxygen white dwarf (WD) and a nondegenerate star or another WD. Here, we present results from high-cadence monitoring observations of SN 2021hpr in a spiral galaxy, NGC 3147, and constraints on the progenitor system based on its early multicolor light-curve data. First, we classify SN 2021hpr as a normal SN Ia from its long-term photometric and spectroscopic data. More interestingly, we found a significant "early excess" in the light curve over a simple power-law  $\sim t^2$  evolution. The early light curve evolves from blue to red to blue during the first week. To explain this, we fitted the early part of the *BVRI*-band light curves with a two-component model consisting of ejecta–companion interaction and a simple power-law model. The early excess and its color can be explained by shock-cooling emission due to a companion star having a radius of  $8.84 \pm 0.58 \, R_{\odot}$ . We also examined Hubble Space Telescope preexplosion images, finding no detection of a progenitor candidate, consistent with the above result. However, we could not detect signs of a significant amount of stripped mass from a nondegenerate companion star ( $\lesssim 0.003 \, M_{\odot}$  for H $\alpha$  emission). The early excess light in the multiband light curve supports a nondegenerate companion in the progenitor system of SN 2021hpr. At the same time, the nondetection of emission lines opens the door for other methods to explain this event.

*Unified Astronomy Thesaurus concepts:* Type Ia supernovae (1728); White dwarf stars (1799); Supernovae (1668); Astrophysical explosive burning (100); Transient sources (1851); Time domain astronomy (2109)

Supporting material: data behind figures, machine-readable table

#### 1. Introduction

The progenitor of Type Ia supernovae (SNe Ia) is expected to be a close binary system of a carbon/oxygen white dwarf (WD). There are two leading models for the progenitor systems of SNe Ia. One is the single degenerate (SD) model. In the SD model, SNe Ia explosion can result from thermonuclear runaway in the WD when the matter from its nondegenerate donors such as a main-sequence (MS), a subgiant (SG), a red giant (RG), or a helium star transfers its material via a Roche lobe until he mass of WD approaches the Chandrasekhar mass of  $M_{\rm ch} \sim 1.4\,M_{\odot}$  (Whelan & Iben 1973; Nomoto 1982; Iben & Tutukov 1984; Hachisu et al. 1996; Wang et al. 2014). The other model, the double-degenerate (DD) model, predicts that a binary WD system can merge via emitting gravitational wave radiation to produce an SN Ia (Webbink 1984; Iben & Tutukov 1984).

Original content from this work may be used under the terms of the Creative Commons Attribution 4.0 licence. Any further distribution of this work must maintain attribution to the author(s) and the title of the work, journal citation and DOI.

SNe Ia have an empirical relation between the width of the light curve and the peak luminosity (width–luminosity relation; Phillips 1993). This allows SNe Ia to be a good tool, a standardizable candle, for measuring distances and probing the expansion history of the universe (Riess et al. 1998; Perlmutter et al. 1999).

Despite its usefulness for various astrophysical applications, SNe Ia progenitor systems are yet to be determined. One of the ways to constrain the progenitor system is to detect shockheated cooling emission (SHCE) in the early-time light curves of SNe Ia after shock breakout (Kasen 2010; Rabinak & Waxman 2011; Piro & Nakar 2013). For the SD scenario, materials in the ejecta are heated by the shock, which is produced from the collision between the ejecta and companion star (Kasen 2010). While the ejecta expand and cool down, the emission (SHCE) can be detected at ultraviolet (UV)/optical wavelengths. The brightness and duration of the SHCE depend on the radius of the companion and the viewing angle from the observer. For a 1  $M_{\odot}$  MS companion, the SHCE would peak at B = -14 AB magnitude while an RG companion ( $\sim$ 143  $R_{\odot}$ )

would produce it with  $B \sim -18$  AB magnitude a day after the explosion. Therefore, according to this picture, the luminosity of any "early excess" in the rising part of the SN Ia light curve can possibly constrain the companion star size (e.g., see Im et al. 2019). The predicted SHCE is in general weak and lasts only for a few hours to days.

There are other ways to produce this early excess without invoking a shock via a companion. If a sub- $M_{\rm ch}$  WD has a helium shell, helium detonation in the shell can induce a shock wave traversing the carbon/oxygen core and trigger a second detonation in the CO core (double detonation or DDet; Woosley et al. 1986). A sub- $M_{\rm ch}$  CO WD with a thin helium shell model (<0.1  $M_{\odot}$ ) is favored in many recent simulations (Fink et al. 2007, 2010; Pakmor et al. 2013; Polin et al. 2019) to explain a significant fraction of subluminous and normal SN Ia events. DDet models predict early excess due to high-velocity nickel coming from helium detonation (Polin et al. 2019). Polin et al. (2019) show that the color evolution during this early excess phase would have a red color peak ("red bump").

Piro & Morozova (2016) predicted the early excess of SNe Ia with various distributions of radioactive nickel (<sup>56</sup>Ni) in the exploding WD and the presence of circumstellar material (CSM) around the primary WD. A shallow <sup>56</sup>Ni distribution (highly mixed) and an extended CSM density can result in a bluer color evolution in the early phase. Magee & Maguire (2020) investigated that <sup>56</sup>Ni shells in the outer ejecta can also produce an early excess in the light curve.

A recent model suggests the early excess can also be seen in DD systems. Levanon et al. (2015) predicted that UV/blue early emission can result from the interaction of SN ejecta and disk-originated matter (DOM), which forms an accretion disk surrounding the primary WD after the companion WD is tidally disrupted.

Observational studies show a diverse nature of SNe Ia early light curves. In some SNe Ia, no early excess is found, disfavoring the SD scenario. Nugent et al. (2011) constrained the progenitor radius of SN 2011fe as  $<0.1\,R_\odot$  with the fireball model ( $t^2$ ). Bloom et al. (2012) gave a tighter constraint on the companion size of  $<0.02\,R_\odot$ , favoring a DD system (but see Mazzali et al. 2014 for a looser constraint). Some studies left the possibility of the SD model, ruling out an RG companion for SN 2012ht (Yamanaka et al. 2014), SN 2017cfd (Han et al. 2020), and SN 2019ein where no early excess was reported (Kawabata et al. (2020) and G. Lim et al., in preparation).

However, there are a number of studies showing a signature of early excess. Marion et al. (2016) constrained the companion mass of SN 2012cg as a  $6 M_{\odot}$  MS binary companion using its early light curve and color evolution. But, other analyses of SN 2012cg favor a DD system for its progenitor (Maguire et al. 2016; Liu & Stancliffe 2016; Shappee et al. 2018). Hosseinzadeh et al. (2017) detected a blue bump for SN 2017cby, inferring the presence of an SG companion of  $56 R_{\odot}$ , although there is an aspect that the companion model does not fully describe the data. Im et al. (2015) found a possible signal  $(2\sigma)$  of SHCE for SN 2015F. Levanon & Soker (2019) suggested the DOM model can explain the linearly rising flux at the early time of SN 2018oh better than the companion model. iPTF14atg (Cao et al. 2015) and MUSSES1604D (Jiang et al. 2017), with an early UV flash and a red bump, are classified as a peculiar and a normal event with other peculiar features, respectively. SN 2018aoz (Ni et al. 2022) and SN 2021aefx (Ashall et al. 2022; Hosseinzadeh et al. 2022), two normal SNe Ia, showed early excess in their light curves, and various models are invoked to explain this early excess. Clearly, there is a need for more early light-curve samples to understand better the SNe Ia progenitor system.

Another way to constrain the progenitor model of SNe Ia is to detect spectral features resulting from companion matter stripped/ablated by the ejecta (Wheeler et al. 1975; Chugai 1986). These features include hydrogen Balmer lines (e.g.,  $H\alpha$ ) and helium emission lines in the optical, which are expected to be seen after the SN enters the nebular phase (\$\ge200\ days; Botyánszki et al. 2018). Marietta et al. (2000) predicted the mass of stripped matter with a numerical simulation as  $0.15-0.17 M_{\odot}$  for MS  $(820 \,\mathrm{km \, s^{-1}})$  SG  $(890 \,\mathrm{km \, s^{-1}})$  stars, and  $0.53 - 0.54 \,M_{\odot}$  for a RG companion star. Meng et al. (2007) also obtained a similar result. Many studies have investigated nebular spectra of SNe Ia, but estimating the mass of unbound material has been challenging (Leonard 2007; Lundqvist et al. 2015; Tucker et al. 2019). Maguire et al. (2016) found possible H $\alpha$  emission for SN 2013ct (corresponding to  $\sim 0.007 M_{\odot}$ ) but no detection for the other 10 SNe Ia in their sample.

As an attempt to enlarge the sample of SNe with early light curves, we have been carrying out the Intensive Monitoring Survey of Nearby Galaxies (IMSNG; Im et al. 2019). IMSNG monitors 60 nearby galaxies with a relatively high SN rate at a cadence less than a day. Among the target galaxies is NGC 3147, where a SN Ia, SN 2021hpr, was discovered (Itagaki 2021). In this paper, we analyze the early, multiband light curve of SN 2021hpr to constrain the explosion mechanism of SN 2021hpr with the focus given mainly to the SHCE model. Additionally, we report the result from latephase spectroscopy of SN 2021hpr using the 9.2 m Hobby–Eberly Telescope (HET) to find the Balmer emission lines that are expected to appear in the nebular phase for the SD model. All the magnitudes, other than quoted explicitly, are in the AB system.

This paper is structured as the following. We present the observations, the data, and the data reduction procedures in Section 2. Section 3 shows the analysis results of the long-term and early light curves, spectral evolution, search for the SN progenitor in Hubble Space Telescope (HST) data, and deep spectroscopy for finding nebular emission lines. In Section 4, we discuss our main findings and demonstrate a wide variety of SN Ia early color curves, which may hint at various explosion mechanisms for SNe Ia. Finally, we summarize our results in Section 5. We use an  $H_0$  value of  $70 \, \mathrm{km \, s^{-1} \, Mpc^{-1}}$  (Hicken et al. 2009; Planck Collaboration et al. 2016). We also neglect K corrections in our analysis since the redshift of NGC 3147 is very low at z = 0.009346 (Tomasella et al. 2021).

#### 2. Observations and Data

#### 2.1. Imaging Observations and Data

SN 2021hpr was discovered on 2021 April 2.45 UT (Itagaki 2021), and classified as a SN Ia (Tomasella et al. 2021). Here, we report our IMSNG imaging observations and the data reduction procedures. In addition, we also used the data in the literature such as those taken at Caucasian Mountain Observatory (CMO; Tsvetkov et al. 2021) and by the Zwicky Transient Facility (ZTF; Bellm et al. 2019). We will describe how their data were transformed to our photometry system.

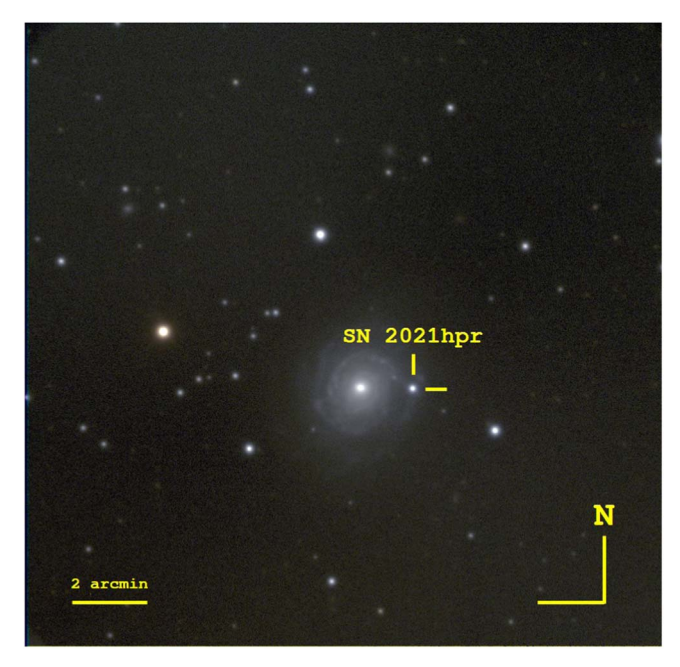


Figure 1. A color composite image of SN 2021hpr in NGC 3147. This image is composed of R- (red), V- (green), and B- (blue) band images observed on 2021 April 17 (almost at B maximum) taken with the DOAO 1 m telescope. The yellow reticle points to the SN. North is up, and east is to the left.

Most of the data come from IMSNG. IMSNG monitoring observations provide data to  $5\sigma$  depths of  $R \sim 19.5$  mag for a point source detection using a network of 0.4-1.0 m class telescopes around the world.

NGC 3147 has been monitored by IMSNG since 2014 in the B and R bands (Figure 1). In our data, SN 2021hpr was first identified in B- and R-band images taken on 2021 April 1.29 (UT) with the 1 m telescope of the Mt. Lemmon Optical Astronomy Observatory (LOAO; Im et al. 2019), located in the USA, after the last nondetection on 2021 March 31.18 with  $3\sigma$ upper limits of B = 20.67 mag and R = 20.18 mag. Our first detection epoch precedes the discovery epoch of Itagaki (2021) by 1.1 days. The IMSNG data were taken nearly daily in the beginning, and then several times a day since the SN discovery up to +30 days from the B-maximum brightness of SN 2021hpr using the *BVRI* bands.

In addition to the LOAO 1.0 m telescope, we used the 0.6 m telescope at the Mt. Sobaek Optical Astronomy Observatory (SOAO), the 1.0 m telescope at the Seoul National University Astronomical Observatory (SAO), the 0.6 m telescope at the Chungbuk National University Observatory (CBNUO), the 1.0 m telescope at the Deokheung Optical Astronomy Observatory (DOAO) in Korea, and SNUCAM (Im et al. 2010) of the 1.5 m telescope at the Maidanak Astronomical Observatory in Uzbekistan (MAO; Ehgamberdiev 2018). Only BVR-band data were obtained at CBNUO and MAO. Refer to Table 2 in Im et al. (2019) and Table 1 in Im et al. (2021) for a detailed description of the facilities. For the SAO observations, we used the Finger Lake Instrumentation (FLI) KL4040 sCMOS camera. Each single exposure time varies with the observatory from 60 to 180 seconds.

Standard reduction (bias, dark subtraction, and flat fielding) procedures were applied to the observed data using the PyRAF (Science Software Branch at STScI 2012) and the Astropy packages (Astropy Collaboration et al. 2013). Additionally, we made a fringe pattern correction to the LOAO I-band data as

described in Jeon et al. (2010). The astrometry calibration was conducted using astrometry.net (Lang et al. 2010).

We performed photometry on images stacked from frames taken consecutively at a similar epoch (3 to 5 frames). The observation time of each combined image is defined as the median of the observing start times of each single frame used for stacking.

We subtracted a reference image from science images using HOTPANTS (Becker 2015), where reference images had been created in advance using images taken with the same telescope and instrument under the best observing conditions. Aperture photometry was performed on the subtracted images using SExtractor (Bertin & Arnouts 1996) with an aperture diameter of 3 × FWHM of the point-spread function (PSF).

The photometric calibration was conducted using stars from Data Release 1 (DR1) of Pan-STARRS<sup>13</sup> (PS1). The selection of the photometry reference stars and the calibration procedures are as follows:

- (i) Extended sources, QSOs, variables, and transients were removed as flagged in the PS1 catalog within the field of view of each image. For CBNUO, we used sources around the image center within a radius of 75% of the field of view to avoid systematic errors that may arise from image distortion around the edges.
- (ii) We further improved the point source selection by selecting sources with i\_PSFmag-i\_Kronmag < 0.05.14 The PS1 magnitudes were transformed into the Johnson BVRI system using equations of the form of  $y = B_0 + B_1 x$ , using coefficients  $B_0$  and  $B_1$  in Table 6 of Tonry et al. (2012) as

$$(B - g_{PS1}) = 0.213 + 0.587(g - r)_{PS1}(\sigma_B = 0.034),$$
 (1)

$$(V - r_{PS1}) = 0.006 + 0.474(g - r)_{PS1}(\sigma_V = 0.012),$$
 (2)

$$(R - r_{PS1}) = -0.138 - 0.131(g - r)_{PS1}(\sigma_R = 0.015),$$
 (3)

$$(I - i_{PS1}) = -0.367 - 0.149(g - r)_{PS1}(\sigma_I = 0.016).$$
 (4)

(iii) Next, we selected stars with transformed magnitudes ranging<sup>15</sup> from 13.5 to 17 with signal-to-noise ratios (S/Ns) larger than 10 and SExtractor FLAG=0. The magnitude zeropoints and their errors were taken as the mean and standard deviation of the zero-points of the reference stars. Typical zeropoint errors are 0.005-0.185 mag depending on the filter and weather conditions.

For the CMO data taken in the SDSS filter system, their griband magnitudes were transformed into BR-band magnitudes using the equations in Table 2 of Blanton & Roweis (2007)

$$B = g + 0.2354 + 0.3915[(g - r) - 0.6102](\sigma_{g-r} = 0.15),$$
(5)

$$V = g - 0.3516 - 0.7585[(g - r) - 0.6102](\sigma_{g-r} = 0.15),$$
(6)

$$R = r - 0.0576 - 0.3718[(r - i) - 0.2589](\sigma_{r-i} = 0.10),$$
(7)

<sup>13</sup> https://catalogs.mast.stsci.edu/panstarrs/

<sup>14</sup> https://outerspace.stsci.edu/display/PANSTARRS/How+to+separate +stars+and+galaxies

15 Bright sources (<13.5 mag) in the PS1 catalog are known to be saturated

<sup>(</sup>Magnier et al. 2013).

				-		
	DOAO (mag)	SAO (mag)	CBNUO (mag)	SOAO (mag)	MAO (mag)	CMO (mag)
	(mag)	(mag)	(11146)	(mag)	(mag)	(mag)
В	-0.138	-0.055	-0.013	-0.075	-0.012	0.069
V	-0.108	-0.059	-0.082	-0.051	-0.050	-0.059
R	-0.127	-0.107	-0.103	-0.047	-0.072	-0.106
I	-0.107	-0.031				0.184

$$I = i - 0.0647 - 0.7177[(i - z) - 0.2083](\sigma_{i-z} = 0.10).$$
(8)

We used the V-band magnitudes presented in Tsvetkov et al. (2021). For the ZTF photometry, we first converted the  $g_{\rm ZTF}$  and  $r_{\rm ZTF}$ -band magnitudes into the PS1 filter system using the equations in Medford et al. (2020). These equations are expressed in terms of  $g_{\rm PS1}$  and  $r_{\rm PS1}$  in this study

$$g_{\text{PS}1} = 0.948g_{\text{ZTF}} + 0.052r_{\text{ZTF}} + 0.011(\sigma_g = 0.004),$$
 (9)

$$r_{\text{PS1}} = 0.076g_{\text{ZTF}} + 0.924r_{\text{ZTF}} + 0.004(\sigma_r = 0.063).$$
 (10)

These ZTF-to-PS1 converted magnitudes were again transformed into BVR-band magnitudes in the same way as above.

We also cross-calibrated the photometry from different telescopes and references. We found that the magnitudes between LOAO and the other telescopes showed slight but significant systematic offsets (Table 1). The magnitude shifts were calculated by subtracting the LOAO magnitudes from the other telescopes' magnitudes in each band after the interpolation. Then, median values were added to the corresponding magnitudes to homogenize the magnitudes to the LOAO photometry. We did not calibrate the ZTF magnitudes since their photometric uncertainties are much larger than their magnitude differences.

#### 2.2. SAO Spectroscopy

We performed long-slit spectroscopy on 2021 April 6, 14, and May 2 at SAO. We used the Shelyak LISA spectrograph with a grating of 300 g/mm and a 2".47 (50  $\mu$ m) slit width. The slit angle was adjusted not to include the nucleus of NGC 3147. Bias, dark, and flat corrections by applying standard IRAF procedures were conducted on the observed spectra. An Ne lamp was used for the wavelength calibration. Flux calibration was conducted using two standard stars, HR 4554 (A0V) and BD+75d 325 (O5P). A log of the SAO spectroscopy is provided in Table 3. The classification and spectral evolution of SN 2021hpr will be discussed in Section 3.5.

#### 3. Results

#### 3.1. Long-term Optical Light Curve

Table 2 provides the optical light-curve data before a dust extinction correction has been applied, and Figure 2 shows the optical light curve from -17.025 to 29.329 days from B maximum, corrected for Galactic and host extinction. Galactic reddening is adopted as  $E(B-V)_{\rm MW}=0.021$  ( $A_B=0.088$ ,  $A_V=0.067$ ,  $A_R=0.053$ , and  $A_I=0.037$ ; Schlafly & Finkbeiner 2011). The host galaxy reddening is determined from the peak B-V color as described in Section 3.2, and we assumed a Galactic extinction curve (Fitzpatrick 1999) and  $R_V=3.1$  to

Table 2
Optical Light Curve of SN 2021hpr with No Extinction Correction Applied

MJD	Phase (day)	Magnitude (mag)	$\sigma_{ m Mag}$ (mag)	Telescope
		B band		
59256.85	-65.01	>21.12		6
59258.77	-63.09	>22.91		6
59259.83	-62.02	>23.07	•••	6
59260.76	-61.10	>23.07	•••	6
59261.71	-60.15	>23.00	•••	6
59262.73	-59.12	>22.28	•••	6
59275.26	-46.59	>19.89	•••	1
59276.53 59277.26	-45.33 -44.60	>20.31		1 1
59217.26	-41.60 -41.60	>21.62 >21.78		1
59283.33	-38.53	>21.76		1
59288.34	-33.51	>21.65		1
59295.12	-26.74	>20.78		1
59298.48	-23.38	>17.57		5
59298.48	-23.38	>17.69		3
59301.16	-20.70	>20.24	• • •	1
59302.21	-19.64	>19.45	•••	1
59303.27	-18.59	>19.76	•••	1
59303.54	-18.31	>18.09	•••	5
59304.18	-17.68	>20.67		1
59304.92 59305.29	-16.94 -16.57	19.35 18.72	0.06 0.41	7 8
59305.29	-16.56	18.75	0.09	1
59306.27	-15.58	18.02	0.04	1
59307.16	-14.69	17.87	0.20	8
59308.22	-13.63	17.22	0.04	1
59308.38	-13.47	17.08	0.04	1
59308.57	-13.29	17.11	0.13	2
59308.65	-13.21	17.08	0.11	4
59309.21	-12.65	16.50	0.03	1
59309.34	-12.52	16.41	0.04	1
59309.47	-12.38	16.49	0.03	3
59309.54	-12.32	16.22 16.09	0.07	5 7
59309.71 59310.19	-12.15 $-11.66$	15.89	0.03 0.04	1
59310.26	-11.60	15.86	0.03	1
59310.34	-11.52	15.82	0.04	1
59310.47	-11.39	15.87	0.05	2
59310.63	-11.23	15.82	0.01	3
59310.64	-11.21	15.80	0.04	4
59311.19	-10.67	15.45	0.04	1
59311.34	-10.52	15.41	0.04	1
59311.63	-10.23	15.39	0.02	4
59311.64	-10.22	15.29	0.06	5 7
59311.82 59312.17	-10.04 -9.69	15.20 15.12	0.03 0.06	1
59312.17	-9.50 -9.50	15.12	0.05	1
59312.52	-9.33	15.16	0.02	3
59312.72	-9.13	14.98	0.01	6
59312.78	-9.08	14.90	0.03	7
59313.23	-8.63	14.86	0.04	1
59313.39	-8.46	14.83	0.04	1
59313.57	-8.29	14.81	0.04	5
59313.59	-8.26	14.94	0.02	3
59313.72	-8.14	14.68	0.03	7
59314.16	-7.69	14.68	0.07	1
59314.37 59314.48	-7.48	14.65	0.04	1 3
59314.48	−7.38 −7.21	14.80 14.68	0.02 0.03	3 4
59314.65	-7.21 -7.21	14.74	0.03	3
59315.22	-6.64	14.51	0.04	1
59315.39	-6.46	14.53	0.03	1

**Note.** The  $3\sigma$  upper limits are also presented. The rest of this table is provided in an online machine-readable form. We also present the original CMO and ZTF data before magnitude conversion. In the column "Telescope," LOAO, SAO, DOAO, SOAO, CBNUO, MAO, CMO, and ZTF respectively correspond to 1, 2, 3, 4, 5, 6, 7, and 8.

(This table is available in its entirety in machine-readable form.)

<sup>16</sup> https://www.shelyak.com/description-lisa/?lang=en

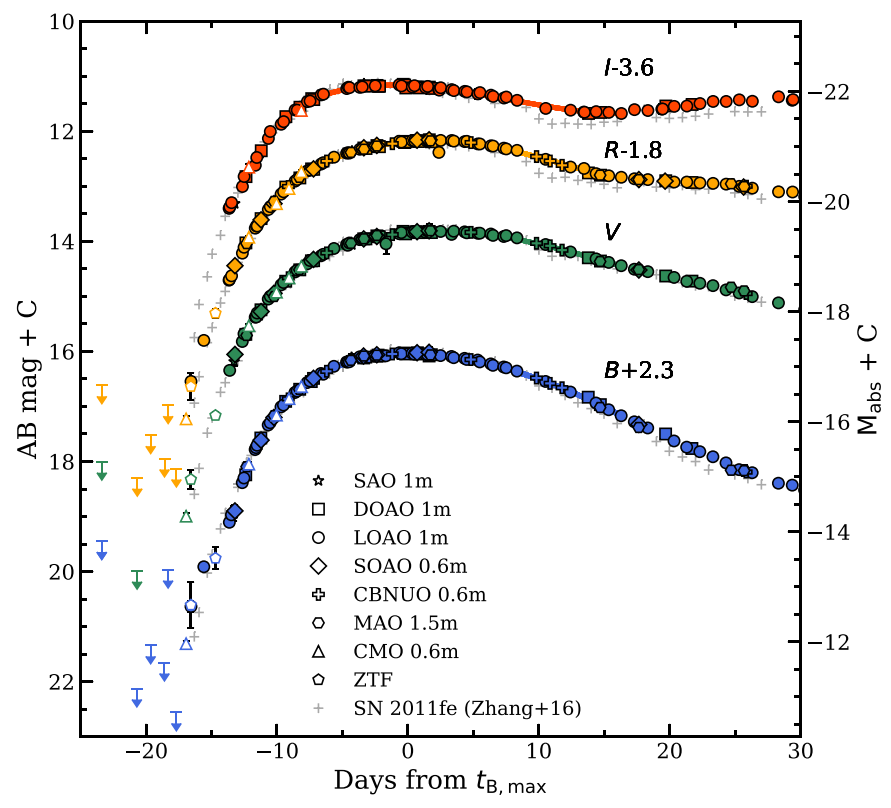


**Figure 2.** The optical light curves of SN 2021hpr. Other reported data points like CMO and ZTF are marked as open symbols. Arrows are  $3\sigma$  upper limits. The polynomial fitting results are overplotted as solid lines. SN 2011fe is also marked as gray cross symbols with an offset to the *y*-axis direction. Corrections for Milky Way and host galaxy extinction have been made.

Table 3
SAO Spectroscopic Observation Log for SN 2021hpr

UT date	Phase <sup>a</sup> (days)	Airmass	Exposure (s)
2021-04-06T14:37:02	-11.3	1.28	2 × 900
2021-04-14T13:55:36	-3.3	1.27	900
2021-05-02T13:09:12	+14.7	1.29	$8 \times 900$

#### Note

obtain the extinction correction in each band. The light curves of SN 2011fe, one of the most well-studied SNe Ia, are overplotted for comparison, matching the *B*-band peak brightness epoch and giving arbitrary *y*-direction shifts to overlap with the maximum brightness of SN 2021hpr. For this, we adopt the SN 2011fe's peak time as 55814.48 MJD (Zhang et al. 2016). A polynomial fit (solid line) was performed on the SN 2021hpr light curve using the data near the peak from -7 to +18 days, which gives us the times and brightnesses ( $t_{\lambda,\max}$ ,  $m_{\lambda,\max}$ ) at the peak brightness and the decline rates,  $\Delta m_{15}(\lambda)$ , at different bands. These quantities are taken from the 50 percentile value in the distribution using bootstrap resampling of the light curves (N=1000; Table 4). The uncertainty is adopted from the standard deviation in the distribution of each parameter.

### 3.2. The Reddening, Peak Absolute Magnitude, and Distance to NGC 3147

We measured the host reddening using the relation between the intrinsic B-V color at maximum brightness,  $(B_{\text{max}}-V_{\text{max}})_0$ , and

 $\Delta m_{15}(B)$  (Phillips et al. 1999). The observed B-V color at maximum brightness,  $(B_{\rm max}-V_{\rm max})_{\rm corr}$ , is  $-0.004\pm0.005$  after correcting for just Galactic extinction. The intrinsic color at maximum brightness,  $(B_{\rm max}-V_{\rm max})_0$ , is expected to be  $-0.083\pm0.040$  for  $\Delta m_{15}(B)=0.988\pm0.026$ . From these values, we measure  $E(B-V)_{\rm host}$  as  $0.079\pm0.040$ . Therefore, the sum of the Milky way and host color excess,  $E(B-V)_{\rm total}$ , is 0.100 (0.021 + 0.079) mag. Note that the reddening of the host is smaller than  $E(B-V)_{\rm host}=0.22\pm0.05$  mag for SN 2008fv (Biscardi et al. 2012), an SN Ia that appeared in another arm of NGC 3147. The extinction values in each band are estimated assuming the Galactic extinction curve ( $R_V=3.1$ ; Fitzpatrick 1999).

In Figure 3, we show previous distance estimates that are derived from historical SNe Ia (Parodi et al. 2000; Reindl et al. 2005; Wang et al. 2006; Prieto et al. 2006; Jha et al. 2007; Kowalski et al. 2008; Takanashi et al. 2008; Amanullah et al. 2010; Biscardi et al. 2012; Tully et al. 2013) and the Tully–Fisher (TF) relation (Bottinelli et al. 1984, 1986; Tully & Fisher 1988). Note that the distances from the TF relation are measured before 1990. These values range from 30 to 50 Mpc with a median value of 41.7 Mpc, and converted to appropriate values adopting a common Hubble constant of 70 km s<sup>-1</sup> Mpc<sup>-1</sup>.

Considering the historical distance (41.7 Mpc), we obtained  $M_{B,\max}$  as  $-19.40 \pm 0.20$ . Figure 4 shows the width–luminosity relation including SNe Ia from the CfA3 catalog (gray dots; Hicken et al. 2009), SN 2021hpr (the yellow star), and SN 2011fe (the blue circle; Zhang et al. 2016). We plot 105 SNe Ia from the CfA3 sample (Hicken et al. 2009) with both photometry and decline rates available in *B* band in the AB system. Since the position of SN 2021hpr is near the Phillips

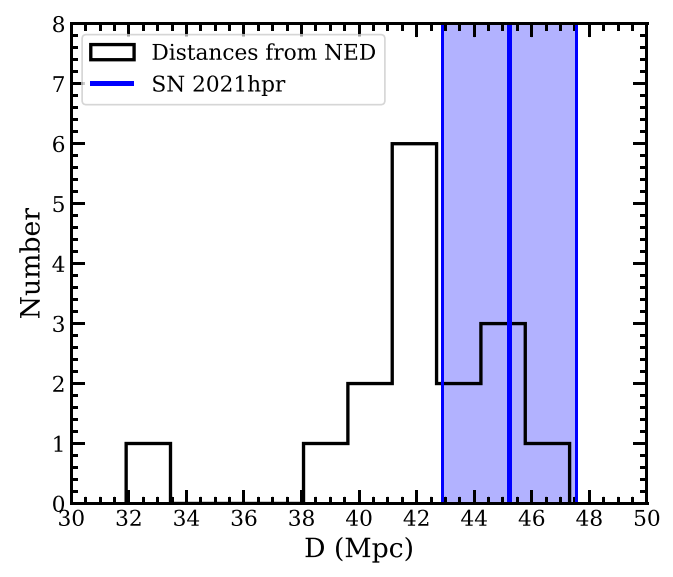
<sup>&</sup>lt;sup>a</sup> Relative to the epoch of *B*-band maximum (59321.864 MJD).

 Table 4

 Light-curve Parameters, Estimated from the Polynomial fit of the Light Curve of SN 2021hpr

	$t_{\lambda,\mathrm{max}} \ \mathrm{(MJD)}$	$m_{\lambda,\mathrm{max}} \ \mathrm{(mag)}$	$\Delta m_{15}(\lambda)$ (mag)	$M_{\lambda,\mathrm{max}} \ \mathrm{(mag)}$	$M_{\lambda,\text{max}}$ (Zhang+22) (mag)
В	$59321.856 \pm 0.218$	$13.724 \pm 0.004$	$0.988 \pm 0.026$	$-19.553 \pm 0.111$	$-19.621 \pm 0.210$
V	$59324.093 \pm 0.127$	$13.811 \pm 0.003$	$0.715 \pm 0.022$	$-19.226 \pm 0.111$	$-19.349 \pm 0.210$
R	$59323.456 \pm 0.124$	$13.973 \pm 0.008$	$0.721 \pm 0.031$	$-19.109 \pm 0.111$	$-19.127 \pm 0.210$
I	$59320.697 \pm 0.137$	$14.762 \pm 0.004$	$0.486\pm0.008$	$-18.400 \pm 0.111$	$-18.595 \pm 0.210$

**Note.** Both Galactic and host extinction corrections have been applied. Also included are the peak absolute magnitudes ( $M_{\lambda, max}$ ) from Zhang et al. (2022). All magnitudes in this table are in the AB system.



**Figure 3.** A histogram of estimated distances to NGC 3147 from the NED database. The distance estimated in this study ( $45.23 \pm 2.31$  Mpc) is marked as the blue solid line shaded with a  $1\sigma$  uncertainty.

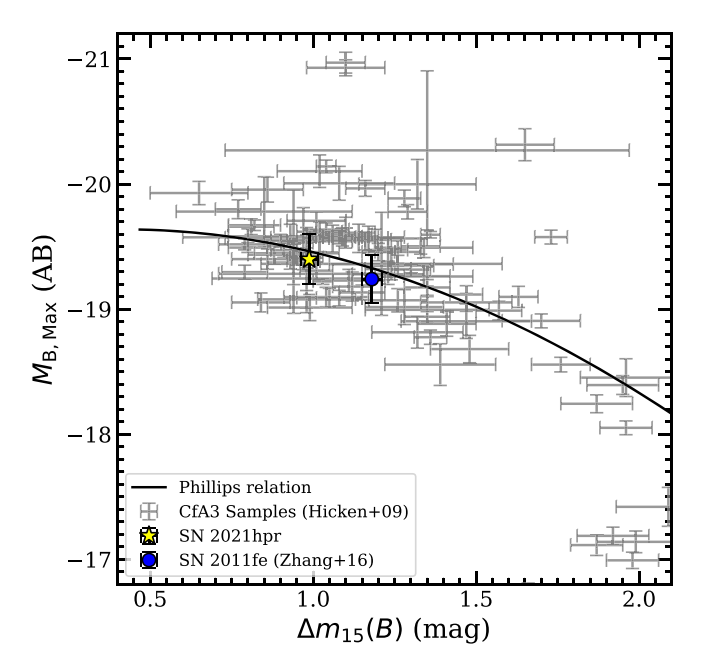


**Figure 4.** The location of SN 2021hpr (a yellow star) in the width–luminosity relation. The Phillips relation is marked in a black solid line. For the  $M_{B,\max}$  value and its error of SN 2021hpr in this plot, we assumed the median distance and its standard deviation from the literature in Figure 2. SNe Ia from the CfA3 catalog are plotted in gray dots with error bars. SN 2011fe is plotted with a blue circle.

relation, we deduce that SN 2021hpr is a normal SN Ia photometrically. Adopting the recent Cepheid distance value from Ward et al. (2022) of 40.1 Mpc ( $\mu = 33.014$  mag) brings the  $M_{B,\text{max}}$  value only by 0.1 mag to the fainter side, and does not affect this conclusion.

Alternatively, we estimate  $M_{B,\max}$  as  $-19.55 \pm 0.11$  AB mag using the decline rate ( $\Delta m_{15}(B) = 0.988 \pm 0.026$ ) from the Phillips relation (Figure 4), which is consistent with a recent measurement in Zhang et al. (2022). We find that the distance modulus ( $\mu$ ) of NGC 3147 is 33.28  $\pm$  0.11 mag, or the distance (d) is  $45.23 \pm 2.31$  Mpc. Our value is a bit larger than the median value of the distribution in Figure 3. However, our value agrees well with 43.70 Mpc derived from a modern day SN Ia, SN 2008fv (Biscardi et al. 2012). In addition, we provide the peak absolute magnitudes from Zhang et al. (2022) in the AB system using their distance modulus of 33.46  $\pm$  0.21 mag to compare our measurements with theirs (Table 4). Our measurements also agree with the value from Zhang et al. (2022) within their errors. For the further analyses, we use a distance modulus of  $\mu = 33.28 \pm 0.11$  mag.

#### 3.3. The Early Light Curve

Figure 5 shows the early light curve of SN 2021hpr  $\pm 5$  days from "the first light time"  $(t_{\rm fl}^{17})$ . In general, the early flux evolution of SNe Ia can be described well with a rising power law  $(t^{\alpha})$  with  $\alpha \sim 2$  (the fireball model; Riess et al. 1998; Nugent et al. 2011), However, SN 2021hpr shows a bumpy feature at very early times  $(t_{\rm fl} < 0)$  that seems to deviate from a simple power-law light curve. Here, we examine this early excess in the light curve quantitatively using a power-law model and the ejecta–companion interaction model suggested by Kasen (2010; K10 hereafter). We modeled the rising part of the SN Ia light curve with the combination of a simple power law and SHCE. The simple power-law model is described in Equation (11)

$$M(t) = M_0 - 2.5\alpha \log_{10}(t - t_{\rm fl}). \tag{11}$$

Here, M(t) is the absolute magnitude as a function of time t, and  $M_0$  is a normalization factor of the absolute magnitude at a unit time of  $t - t_{fl} = 1$  day.

The SHCE light curve is calculated using the ejecta-companion interaction model of K10. To calculate the effective temperature,  $T_{\rm eff}(t)$ , and the luminosity, L(t), of SHCE, we use

<sup>&</sup>lt;sup>17</sup> We adopted the term "the first light time" from Im et al. (2015) describing that the photons generated from the radioactive decay of <sup>56</sup>Ni, which start to escape from the photosphere. The first light time is distinguished from "the explosion time," which is the actual explosion time.

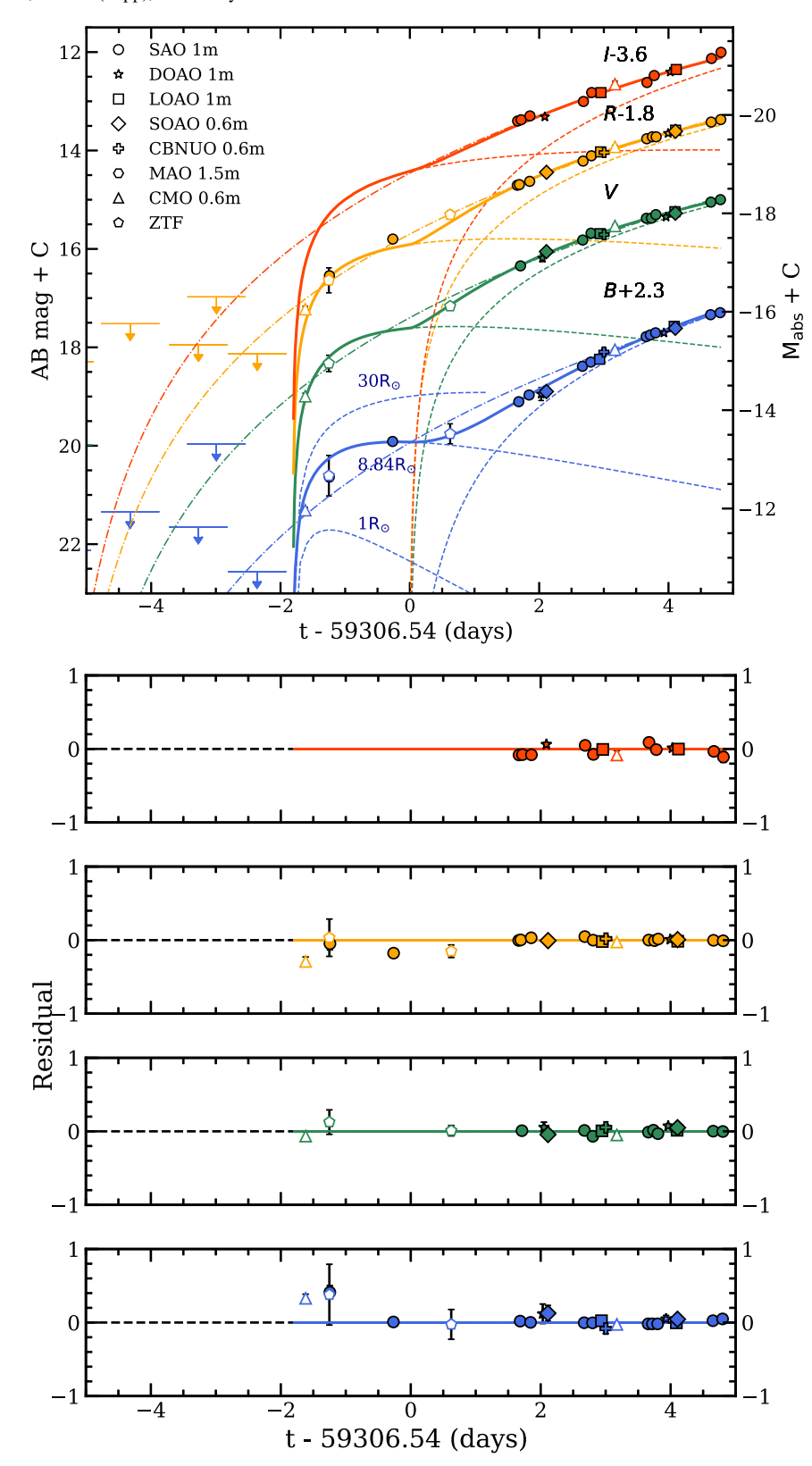


Figure 5. Top: the early light curve of SN 2021hpr between -5 and 5 days from the first light time with the best fit of the two-component model (solid line). The dashed lines show the separated model lines of K10 and the power-law fitting results. K10 models for  $1 R_{\odot}$  and  $30 R_{\odot}$ -sized companion stars are also overplotted (blue dashed lines). Pure simple power-law model lines are also overplotted in dashed–dotted lines. Each symbol is the same as that in Figure 2. Bottom panels: residual plots corresponding to the top panel.

Table 5
The Best Results of the Early Light Curve Fit by Different Methods

Fitting Method	Viewing Angle	$\alpha$	$M_0$ (mag)	$t_{\rm exp} \ ({ m MJD})$	$t_{\rm fl} \ ({ m MJD})$	$t_{\rm gap} \ ({ m days})$	$R_* \ (R_{\odot})$	$\chi^2_{\nu}$
Simple power law		(B) $3.84 \pm 0.32$ (V) $3.56 \pm 0.27$	$24.70 \pm 0.99 \\ 23.95 \pm 0.86$		59301.10			5.0
		(R) $3.45 \pm 0.28$ (I) $3.44 \pm 0.27$	$23.84 \pm 0.88$ $24.38 \pm 0.83$		±0.52			
Companion+simple power law	Optimal	(B) $2.03 \pm 0.13$ (V) $1.48 \pm 0.10$ (R) $1.50 \pm 0.11$ (I) $1.79 \pm 0.13$	$18.44 \pm 0.29$ $17.59 \pm 0.22$ $17.83 \pm 0.23$ $18.99 \pm 0.26$	59304.73 ±0.01	59306.54 ±0.18	1.81 ±0.18	8.84 ±0.58	2.4
	Common	(B) $3.74 \pm 0.28$ (V) $2.74 \pm 0.18$ (R) $2.58 \pm 0.19$ (I) $2.79 \pm 0.20$	$\begin{array}{c} 23.37 \pm 0.78 \\ 21.17 \pm 0.53 \\ 21.02 \pm 0.55 \\ 22.05 \pm 0.56 \end{array}$	59304.30 ±0.11	59303.55 ±0.45	$-0.75 \pm 0.43$	175.59 ±52.71	3.1
Companion+simple power law (Fireball)	Optimal	2 (Fixed)	(B) $18.85 \pm 0.06$ (V) $18.79 \pm 0.06$ (R) $19.01 \pm 0.05$ (I) $19.70 \pm 0.05$	59304.70 ±0.03	59305.60 ±0.13	0.91 ±0.13	6.52 ±1.09	5.3

Note. We did not include the case of the companion+simple power-law model (fireball) assuming a common viewing angle because we obtained an unacceptable result where the model lines cannot explain the upper limits in the observed data.

the equations below which are taken from Im et al. (2015)

$$T_{\rm eff}(t) = 5.3 \times 10^3 \frac{R_{10}^{1/4}}{\kappa_{0.2}^{35/36}} t_{\rm exp}^{-37/72} \,\mathrm{K},$$
 (12)

$$L(t) = 2.0 \times 10^{40} \frac{R_{10} M_c^{1/4} v_9^{7/4}}{\kappa_{0.2}^{3/4}} t_{\rm exp}^{-0.5} \,\rm erg \, s^{-1}. \tag{13}$$

Here,  $R_{10}$  is the radius of the companion star in units of  $10^{10}$  cm  $(R_{10} = R_*/10^{10}$  and  $R_* = a/2$ , where a and  $R_*$  are the separation distance and stellar radius, respectively),  $\kappa_{0.2}$  is the opacity in units of 0.2 cm<sup>2</sup> g<sup>-1</sup>, which is adopted as 1.0,  $M_c$  is the ejecta mass in units of 1.4  $M_{\odot}$ , which is adopted as 1/1.4,  $t_{\rm exp}$  is the time since the explosion in units of days, and  $v_9$  is the expansion velocity of the ejecta in units of  $10^9$  cm s<sup>-1</sup> (adopted as 1.0 here).

The light-curve fit was performed on the four bands of data simultaneously by minimizing  $\chi^2$  using the Python library of LMFIT (Newville et al. 2014). The fitting was performed using the data points from MJD = 59304.92 to 59311.35, i.e., all the detection points presented in Figure 5. The free parameters are  $\alpha_{\rm B}$ ,  $\alpha_{\rm V}$ ,  $\alpha_{\rm R}$ ,  $\alpha_{\rm I}$ ,  $M_{\rm 0,B}$ ,  $M_{\rm 0,V}$ ,  $M_{\rm 0,R}$ ,  $M_{\rm 0,I}$ ,  $t_{\rm fl}$ ,  $R_*$ , and  $t_{\rm gap}$ , where the last two parameters are, respectively, the radius of the companion star in units of  $R_{\odot}$  and the time gap between  $t_{\rm exp}$  and  $t_{\rm fl}$  ( $t_{\rm gap} = t_{\rm fl} - t_{\rm exp}$ ), where  $t_{\rm exp}$  is the explosion time, which marks the start of SHCE. Furthermore, the amount of SHCE in the companion model is dependent on the viewing angle. We assume the optimal viewing angle whereby the observer looks at the shocked region along the line of sight (observercompanion-WD), giving the brightest collision luminosity. If we assume a common viewing angle, the companion radius could be larger than that obtained with the optimal viewing angle by about a factor of 10.

The best-fit parameters and the best-fit light curves are given in Table 5 and Figure 5. As seen in Figure 5, our two-component model can explain the early excess of SN 2021hpr with a  $R_* = 8.84 \pm 0.58\,R_\odot$ -sized companion, where the goodness of fit  $\chi^2_\nu$  is 2.4. The explosion time ( $t_{\rm exp}$ ) is estimated as  $59304.73 \pm 0.01\,$  MJD.  $t_{\rm gap}$  is also estimated as

 $1.81 \pm 0.18$  days. This can be regarded as a large value (e.g., Noebauer et al. 2017), but it is acceptable if a large fraction of  $^{56}\mathrm{Ni}$  is deep from the ejecta surface, in which case  $t_{\mathrm{gap}}$  can be up to a few days after the explosion (Piro & Nakar 2013). When assuming a common viewing angle, which we modeled by multiplying Equation (13) by 0.1, the radius of the companion star can be found as  $R_* = 175.59 \pm 52.70 R_{\odot}$  $(\chi_{\nu}^2 = 3.1$ , see the top left panel of Figure A1). When we fix the power index to 2 (the fireball model),  $t_{\rm gap}$  is  $0.91 \pm 0.13$  days and  $R_* = 6.52 \pm 1.09 \, R_{\odot}$ , with  $\chi^2_{\nu} = 5.3$ (optimal viewing angle). A simple power-law model gives a poorer fit ( $\chi_{\nu}^2 = 5.0$ , dashed-dotted line) and a too-large  $\alpha$ . Furthermore, the best-fit  $t_{\rm fl}$  from the simple power-law model is several days before the best-fit  $t_{\rm fl}$  from the two-component model, and the best-fit model curve goes over the  $3\sigma$  detection limits at the last nondetection. Note that the best-fit  $t_{\rm fl}$  from this model is 59301.10  $\pm$  0.52 MJD). Therefore, a simple powerlaw model is disfavored.

#### 3.4. Early Color Evolution

Our multicolor, high-cadence monitoring observations allow us to construct color curves from the time shortly after the explosion. The 2nd and 3rd left panels of Figure 6 shows the color curves of B - V and B - R, for several  $R_*$  values for the power-law+K10 model. SN 2021hpr was blue very early on, then reddened, and then became blue again a few days after the first light time. This overall behavior is in qualitative agreement with our two-component model including SHCE. According to the two-component model, the  $T_{\rm eff}$  of SHCE increases as  $R^{1/4}$ , meaning that the larger the companion is, the bluer the early color curve is. Therefore, in this model, if the companion star is large  $(R_* \sim 30 R_{\odot})$ , the predicted colors are very blue. On the other hand, the peak of the color curve in the early epochs becomes too red if the companion star is too small. Figure 6 shows the early peak colors agree with a rather small companion star case  $(R_* \sim 9 R_{\odot})$ .

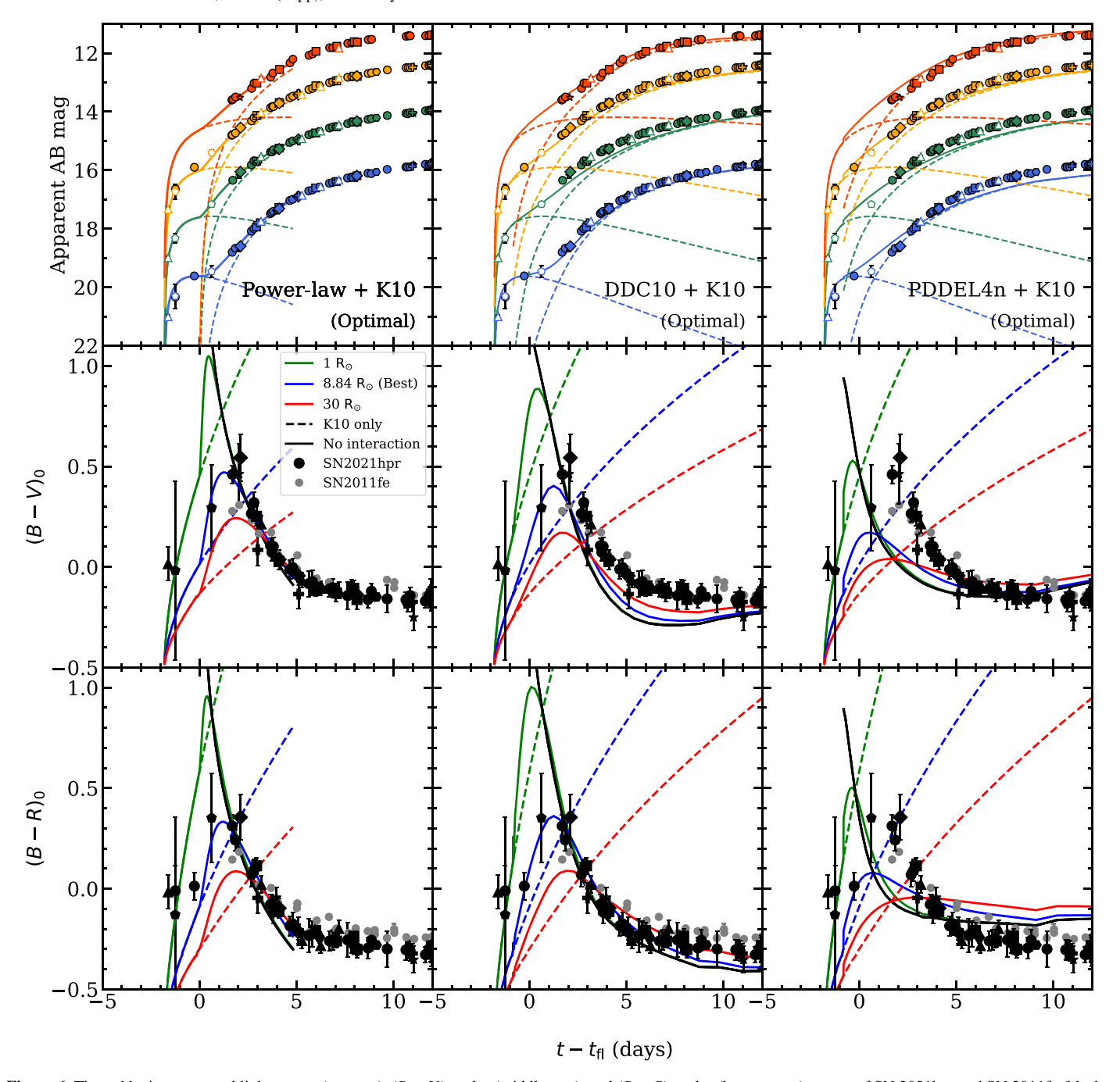


Figure 6. The reddening-corrected light curves (top row),  $(B - V)_0$  color (middle row), and  $(B - R)_0$  color (bottom row) curves of SN 2021hpr and SN 2011fe (black and gray filled circles, respectively) in the early phase with the different two-component models (the best fit of companion+simple power law; DDC10, Blondin et al. 2013; and PDDEL4n, Dessart et al. 2014; at the optimal viewing angle). Two-component models with different companion radii and only K10 models are also presented in solid and dashed lines, respectively.

Additionally, Figure 6 shows the cases where the power-law model is replaced with delayed detonation models (DDC; Khokhlov 1991; Blondin et al. 2013) and pulsational detonation models (PDD; Dessart et al. 2014). These specific models do not include emission from ejecta interaction with a companion star, and can possibly fit the early light curve if an SHCE component is included. The SHCE component is taken as the one that best fits the observed data.

The DDC models of Blondin et al. (2013) are controlled mainly by the transition density  $\rho_{\rm crit}$  at which the deflagration is artificially turned into a detonation. Their DDC10 model mimics the light curve of SN 2021hpr after the very early phase, which

has been chosen for Figure 6. For a similar reason, we plot the PDDEL4n model of Dessart et al. (2014) in Figure 6, which is also know to reproduce SN 2011fe's properties.

When combined with the SHCE model, both the DDC10 and PDDEL4n models reproduce the early light and color curve behavior qualitatively, although the PDDEL4n model seems to deviate quantitatively from the observed data. We stress that the comparison is done without any sophisticated fitting procedure, so the PDDEL4n model may provide a reasonable fit to the data when some of the SHCE parameters are adjusted.

We also present other possible results with different configurations in Figure A1, including the cases of the

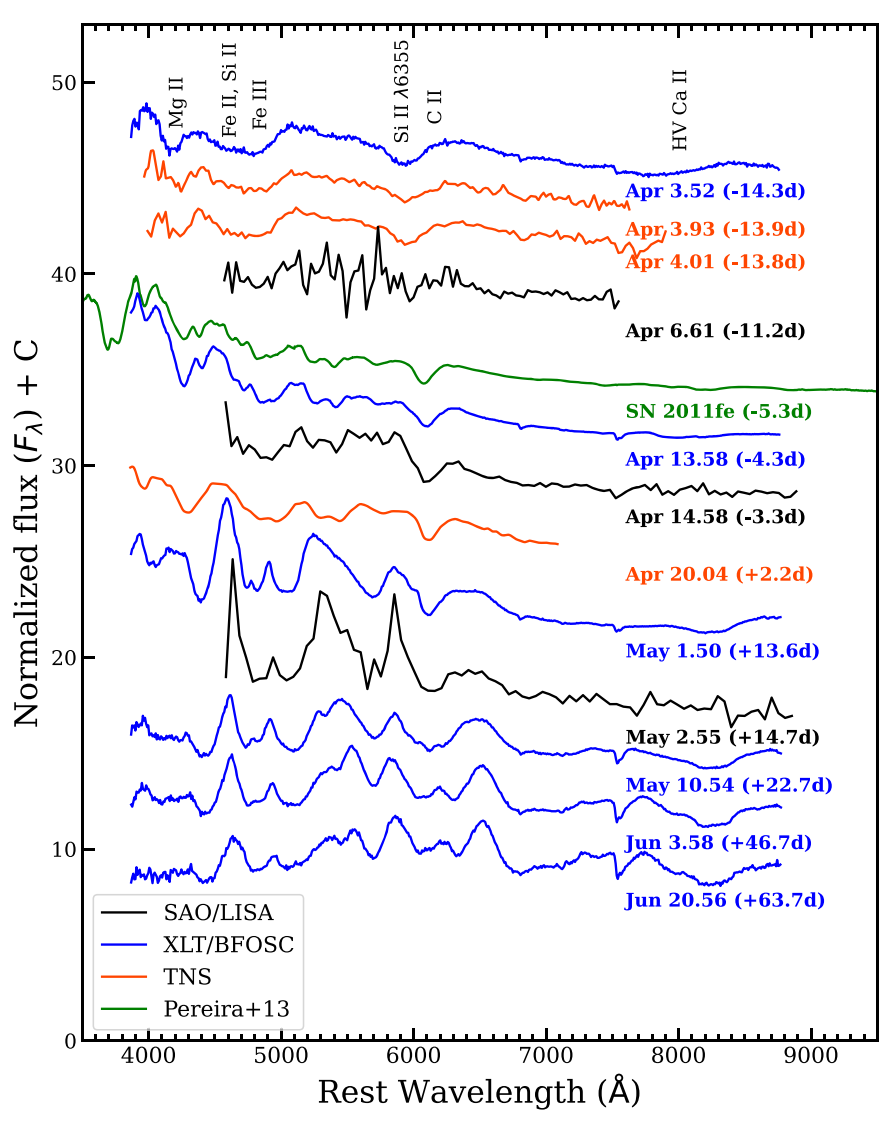


**Figure 7.** Optical spectral evolution of SN 2021hpr observed with multiple instruments including SAO (black), XLT (blue), and TNS (orange-red). The normalized fluxes are shifted by arbitrary constant values. No extinction corrections have been made except for SN 2011fe (green). (The data used to create this figure are available.)

power-law+K10 fit at a common viewing angle and other variants of the DDC models from Blondin et al. (2013) and Dessart et al. (2014). The conclusion we draw from Figure A1 is similar to Figure 6 in that these other models with an SHCE component can qualitatively mimic the early light-curve behavior.

#### 3.5. Optical Spectra and the Nature of SN 2021hpr

To confirm SN 2021hpr's classification, we examined the time evolution of the spectra. Figure 7 shows the optical spectra of SN 2021hpr. For better classification, we additionally include high-quality spectra from the 2.16 m telescope at XingLong Observatory (XLT) and the Transient Name Server<sup>18</sup> (TNS) published in Zhang et al. (2022). We also overplotted a spectrum of SN 2011fe (Pereira et al. 2013) to compare these SNe. The SAO, XLT, and the second TNS spectrum (–13.9 days before peak brightness) were binned to

Table 6
Description of the HST WFC3/UVIS and IR Images

	•		•	_	
		Pre	-SN		Post-SN
Filter	F350LP	F555W	F814W	F160W	F814W
Detector	UVIS	UVIS	UVIS	IR	UVIS
$t_{\rm exp}$ (s)	25,520	5952	5954	12055	780
N of images	11	5	5	5	1
Pivot $\lambda$ (Å)	5862.5	5308.2	8034.2	15369.2	8034.2
$3\sigma$ limit (AB)	>28.10	>28.04	>27.45	>25.41	>26.56
$A_{\lambda, \text{host}}$ (mag)	0.27	0.31	0.16	0.06	0.16
$M_{\rm abs,obs}$ (AB)	> -5.18	>-5.24	>-5.83	> -7.87	> -6.72
$M_{\rm abs,0}~({\rm AB})$	>-5.45	>-5.56	>-6.00	>-7.92	>-6.89

**Note.** Host reddening  $(A_{\lambda,\text{host}})$  is calculated at the pivot wavelength.  $M_{\text{abs},0}$  is the Milky Way and host reddening-corrected absolute magnitude.

10, 3, and 3 pixels, respectively, to increase their S/Ns after  $3\sigma$  clipping. No binning was applied to the other spectra. For the XLT data, we excluded noisy regions <3900 Å.

https://sandbox.wis-tns.org/object/2021hpr

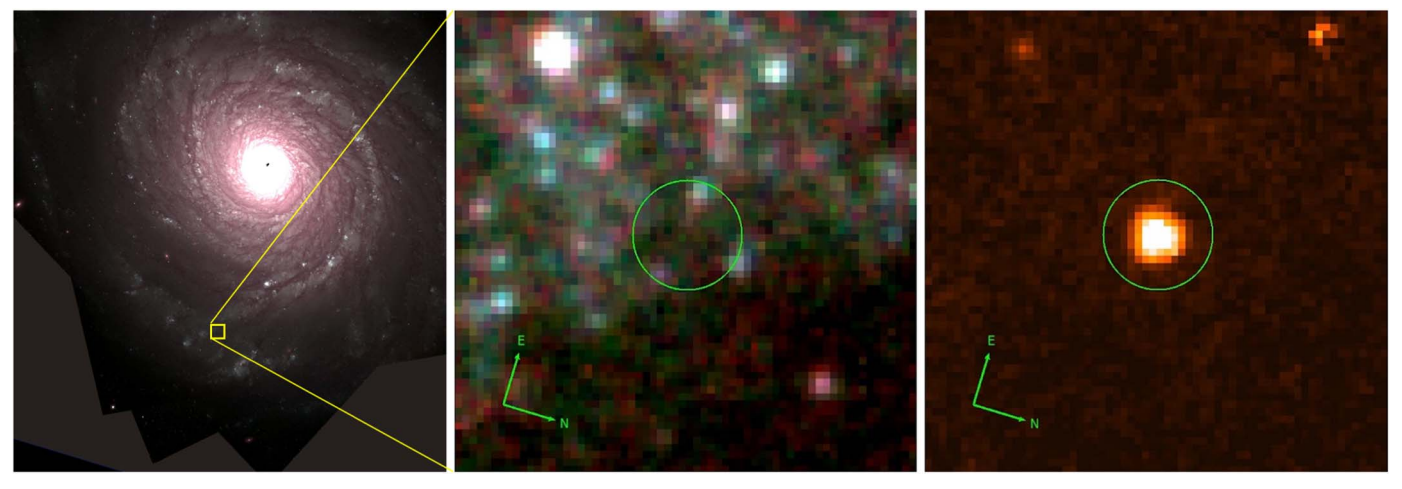


Figure 8. Left: an F350LP/F555W/F814W color image before the explosion of SN 2021hpr observed by HST/WFC3. Middle: a zoomed-in look (2.".5 × 2.".5) of the region in the yellow box of the full-frame image on the left. The site of SN 2021hpr is marked with a green circle centered at the Gaia alert coordinates with a  $1\sigma$  astrometric error radius (0.".3). Right: the detection image of SN 2021hpr in the F814W filter on 2021 December 29. The field of view is the same as the middle panel. The source on the upper right is an artifact.

Zhang et al. (2022) demonstrated that the spectra of SN 2021hpr show many broad features originating from intermediate mass elements (IMEs) such as Si II, Mg II, and highvelocity Ca II absorption lines. Fe features are also seen but unburned carbon feature (C II) is not prominent, which is seen in SN 2011fe. The very high expansion velocity of Si II decreases at a rate of about  $-800 \,\mathrm{km \, s^{-1}}$  per day, making SN 2021hpr classified as a high-velocity gradient group (HVG) SN Ia. In the SAO spectra, we can also find IME features ranging from 4600 to 9000 Å despite their poor S/Ns. Applying the GEneric cLAssification TOol (GELATO; Harutyunyan et al. 2008) to the April 14 spectrum (taken at near maximum brightness), we find that the SN 2021hpr spectrum is similar to SN 1989B, a normal SN Ia. Its width-luminosity relation (Figure 4), the similarity of its light curve to SN 2011fe, and its spectral features all suggest that SN 2021hpr is a normal SN Ia.

We discuss SNe Ia with or without an early flux excess in terms of spectral diversity with some cases. Early flux excesses are found in some luminous SNe Ia (99aa-like) showing weak or no Ca II and Si II absorption features, such as SN 2015bq (Li et al. 2022) and iPTF14bdn (Smitka et al. 2015). Likewise, a subluminous SN Ia, iPTF14atg (Cao et al. 2015), is reported to have an early flux excess at UV wavelengths. MUSSES1604D (Jiang et al. 2017) is a hybrid SN Ia classified as a normal SN Ia in photometry but has a peculiar Ti II absorption feature in its spectra. SN 2017cbv is close to a normal SN Ia with transitional characteristics, such as weak Si II and Ca II absorption features, but stronger than those of 99aa-like SNe Ia (Hosseinzadeh et al. 2017). On the other hand, normal SNe Ia with early flux excesses have also been discovered, such as SN 2012cg (Marion et al. 2016), SN 2018aoz (Ni et al. 2022), SN 2018oh (Li et al. 2019), and SN 2021hpr in this paper.

Unburned carbon features (e.g., C II λ6580) can be found in both SNe Ia with (SN 2012cg, SN 2017cbv, SN 2018oh, and iPTF14atg) and without an early flux excess (SN 2011fe, Pereira et al. 2013; SN 2012ht, Yamanaka et al. 2014; and SN 2013dy, Zheng et al. 2013). High-velocity features (HVFs) near maximum brightness seem to appear in both kinds of SNe Ia with (SN 2021hpr, Zhang et al. 2022; SN 2021aefx, Hosseinzadeh et al. 2022) and without an early flux excess (SN 2012fr, Zhang et al. 2014; Contreras et al. 2018; SN 2019ein,

Kawabata et al. 2020). Further spectroscopic data, especially obtained at early times, are required to understand the relation between spectral features and the early flux excess.

### 3.6. Finding the Possible Progenitor System in Preexplosion HST Images

We can possibly constrain the progenitor system, especially the companion star, by directly identifying it at the SN position in preexplosion images (Li et al. 2011; McCully et al. 2014). We identified a series of HST images from the HST archive  $^{19}$  taken before the SN explosion during 2017 November–2018 March (Proposal 15145, PI: A. Riess) and after the explosion (Proposal 16691, PI: R. Foley). The images were obtained with Wide-Field Camera 3 (WFC3) in the F350LP, F555W, F814W, and F160W filters. Table 6 summarizes the observations. The single frame images were stacked using Swarp (Bertin 2010). Figure 8 shows the HST images before and after the SN explosion. The coordinates of SN 2021hpr and its  $1\sigma$  error, 0."3 from the Gaia alert (Yaron 2019) in TNS, is drawn as a circle in the figure.

At the SN 2021hpr position, no obvious source was found in the preexplosion image. We measured a  $3\sigma$  detection limit for a point source with the default aperture size of a 0."2 radius, finding upper limits on the progenitor system's magnitudes of  $\sim$ 27–28 mag in the optical, and  $\sim$ 25 mag in F160W (Table 6).

Figure 9 shows a color–magnitude diagram (CMD) with stellar evolutionary tracks and HST upper limits. The tracks are calculated from the MESA Isochrones and Stellar Tracks (MIST; Choi et al. 2016), a recent set of stellar evolutionary tracks and isochrones, which provides synthetic photometry in the HST/WFC3 filters. We adopted the tracks for initial masses ( $M_{\rm init}$ ) from 8 to 16  $M_{\odot}$  with a step of 2  $M_{\odot}$  and solar metallicity. We also plotted the Bessell V- and I-band synthetic photometry of some evolved stars, including asymptotic giant

<sup>19</sup> https://archive.stsci.edu/

<sup>20</sup> http://waps.cfa.harvard.edu/MIST/index.html

<sup>&</sup>lt;sup>21</sup> The synthetic photometry values were calculated from a spectral energy distribution (SED) fit of samples in the literature. We plotted the Bessell filter magnitudes because there is no large difference between the *V*- and *I*-band, and F555W- and F814-band magnitudes.

Table 7

The RMS of the Nebular Features and Flux and Luminosity Limits of the Nebular Emission Lines, Along with the Upper Limits on the Stripped Mass Corrected by Multiplying the Correction Factors Expected at +250 Days Since Explosion

Line	$W_{ m line} \ ( m \AA)$	Nebular Flux Noise ( $\sigma$ ) ( $10^{-17}$ erg Å <sup>-1</sup> cm <sup>-2</sup> s <sup>-1</sup> )	Flux Limit $(3\sigma)$ $(10^{-16} \text{ erg } \mathring{A}^{-1} \text{ cm}^{-2} \text{ s}^{-1})$	Luminosity Limit $(3\sigma)$ $(10^{38} \text{ erg s}^{-1})$	$M_{\rm st}$ Limit $(M_{\odot})$
$H\alpha$	21.89	1.29	8.48	2.08	< 0.003
$H\beta$	16.22	1.97	9.60	2.35	< 0.003
$H\gamma$	14.48	4.60	19.99	4.89	< 0.005
He I $\lambda 5876$	19.60	1.86	10.93	2.68	< 0.003
He I $\lambda 6678$	22.28	0.95	6.37	1.56	< 0.002

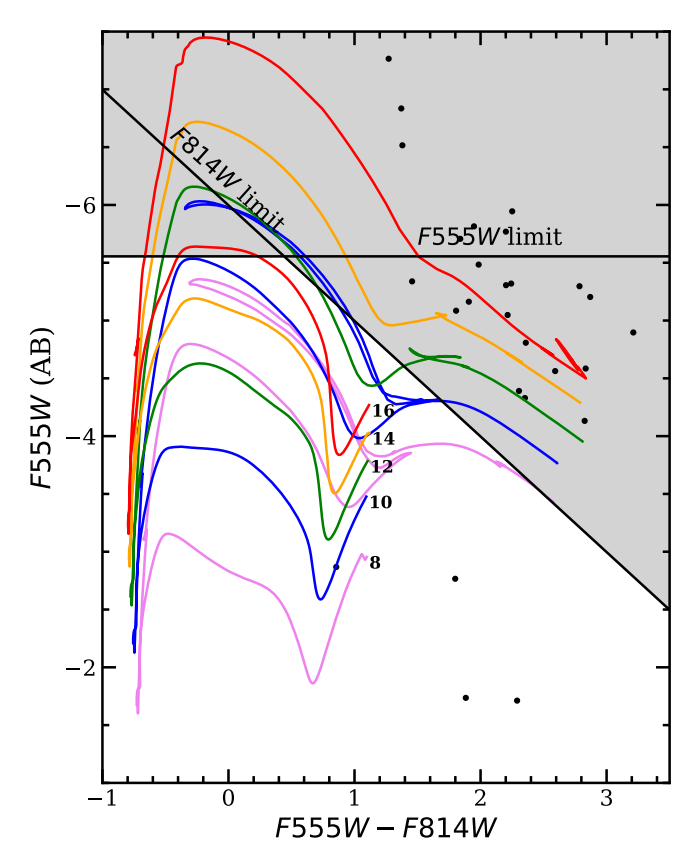


**Figure 9.** A CMD of HST filters with MIST evolutionary tracks for massive stars with initial masses from 8 to  $16\,M_\odot$ , assuming solar metallicity. The initial masses are marked at the starting points of the tracks. The gray shaded area shows the excluded parametric space for the progenitor system based on the HST nondetection. Extinction corrections are applied to derive the upper limits here (the black solid lines). The Bessell synthetic V- and I-band photometry of evolved stars in the LMC are marked as black filled circles.

and supergiant branch stars in the Large Magellanic Cloud (LMC; black filled circles; Groenewegen & Sloan 2018).

In the CMD, stars with  $M_{\rm init} \gtrsim 10\,M_{\odot}$ , except for some in a high-luminosity phase, would have been detected in the HST image. A radius of  $M_{\rm init} \sim 10\,M_{\odot}$  star can be approximated with the evolutionary tracks in Levesque et al. (2005). Assuming  $\log_{10}(T_{\rm eff}[K]) = 3.57$  and  $M_{\rm bol} = -5.0$  mag as the effective temperature and bolometric magnitude of stars with  $M_{\rm init} = 10\,M_{\odot}$ , respectively, we obtain  $L/L_{\odot} \sim 7870$ , giving us  $R_* \sim 215\,R_{\odot}$  as an upper limit of the radius of the companion star.

## 3.7. The Stripped Mass Limit from HET Late-phase Spectroscopy

To identify emission lines from stripped matter from the companion, we also obtained an optical spectrum of SN

2021hpr using the blue pair of the second-generation Low-Resolution Spectrograph (LRS2-B) mounted on the 9.2 m HET at McDonald Observatory, USA (Chonis et al. 2014). LSR2-B is a  $12''\times7''$  integral field unit (IFU) that covers the wavelength ranges  $3700\leqslant\lambda(\mathring{\rm A})\leqslant4700$  ( $R\sim1900$ ) and  $4600\leqslant\lambda(\mathring{\rm A})\leqslant7000$  ( $R\sim1100$ ). A single frame of 1000 seconds was obtained under dark conditions ( $g\sim21.13$  mag arcsec<sup>-2</sup>) on 2021 November 30.26 UT. At that time, SN 2021hpr was in a late phase (59548.26 MJD, +226 days from maximum B brightness).

The spectrum was reduced using the code Panacea,  $^{22}$  the standard pipeline of HET LRS2. Flux calibration was conducted by observing HD 55677 as a spectrophotometric standard and using this spectrum to set the zero-point of the response curve, while the shape of the response curve was constructed from a sequence of standard stars observed over six months in 2019. We used the redshift of z=0.009346 from Tomasella et al. (2021) to shift the spectrum to the rest frame. Milky Way and host galaxy extinctions were also corrected. Furthermore, we recalibrated the flux of the spectrum so that the flux values of the spectrum match our photometry at the observed date by multiplying the flux by 1.9 as a correction factor. It is not clear why the integrated flux from the HET spectrum is different from the value from the image photometry. Varying weather conditions could be the reason.

Figure 10 shows the reduced spectrum. To search for nebular emission lines, we subtracted the SN nebular flux features in the following way. We adopted the method from Tucker et al. (2019) for the nebular flux fit. We first masked regions around spectral lines such as the Balmer series lines (H $\alpha$ , H $\beta$ , H $\gamma$ ), He I  $\lambda$ 5876, and He I  $\lambda$ 6678 with a width of 1000 km s<sup>-1</sup> ( $W_{\rm line}$ ), which is known to be the line width of stripped matter (Marietta et al. 2000; Boehner et al. 2017). Then, the spectrum was smoothed using a second-order Savitzky–Golay polynomial (Press et al. 1992) with a window size of 3000 km s<sup>-1</sup> at 6563 Å, which is wider (narrow) than the host galaxy (ejecta) features. Considering R = 1100 at He I  $\lambda$ 6678, the observed data were binned to a wavelength size of 6 Å. The observed data and the fitted nebular flux are shown as the black and red lines in Figure 10.

After subtracting the best-fit nebular flux from the observed spectrum, we searched for signs of emission lines in the corresponding spectral regions, but no significant emission lines were found (Figure 10). We measured emission line flux limits from the nebular flux rms values around each line, as presented in Table 7. The rms was measured as the standard deviation of the Gaussian fit of the nebular flux distribution ranging from  $-3 \times W_{\text{line}}$ :- $W_{\text{line}}$  to  $W_{\text{line}}$ :3  $\times W_{\text{line}}$ , excluding the signals at the position of each emission line (the gray shaded

https://github.com/grzeimann/Panacea

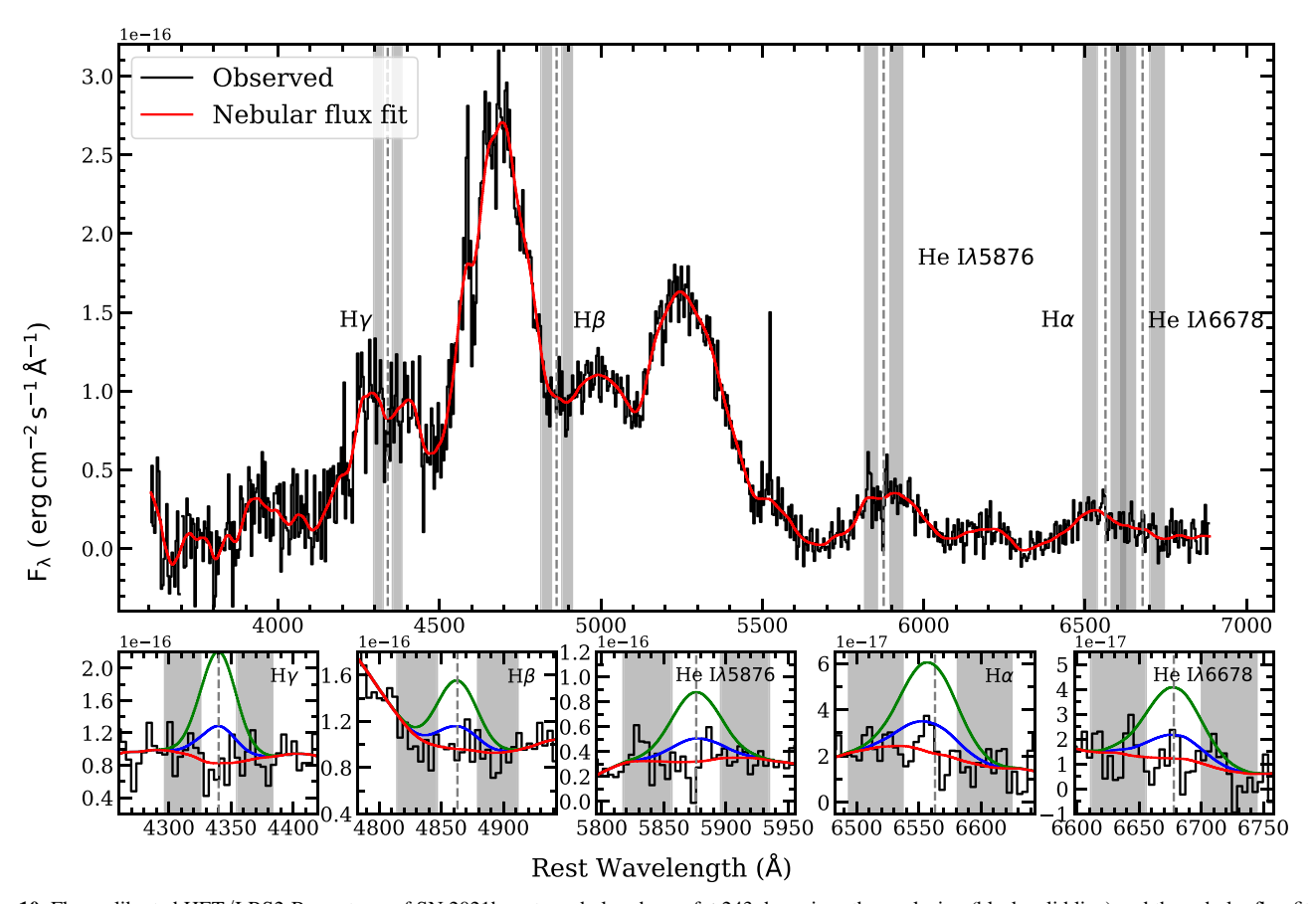


Figure 10. Flux-calibrated HET/LRS2-B spectrum of SN 2021hpr at a nebular phase of  $\pm$ 243 days since the explosion (black solid line) and the nebular flux fit (red solid line). The gray dashed lines mark the positions of each spectral line. The gray shaded areas are regions used for measuring the rms of the nebular flux. The bottom five panels show spectral regions around nebular emission lines and the  $1\sigma$  and  $3\sigma$  line flux limits (blue and green solid lines, respectively). Fluxes are binned at a size of 6 Å.

(The data used to create this figure are available.)

regions in Figure 10). The  $1\sigma$  and  $3\sigma$  flux limits are also plotted together in Figure 10 assuming a Gaussian profile with a width of 1000 km s<sup>-1</sup>. These flux limits are converted into luminosity limits considering the distance to the SN. For the H $\alpha$  emission line, the  $3\sigma$  luminosity limit is  $2.08 \times 10^{38} \, \mathrm{erg \, s^{-1}}$ . Using the  $H\alpha$  luminosity-stripped mass relation of the MS38 model (Equation (1) from Botyánszki et al. 2018), we estimate the  $3\sigma$ stripped mass limit ( $M_{\rm st}$ ) for each emission line.<sup>23</sup> Since this model gives a prediction at 200 days after the explosion, we estimated a scale factor to calculate  $M_{\rm st}$  at +243 days since the explosion. This was done by adopting the luminosity ratio between 200 and 243 days as the scaling factor, since the ratio of the bolometric luminosity to  $H\alpha$  luminosity is known to be constant (Botyánszki et al. 2018). During 200 and 250 days since the explosion, SN 2021hpr was observed in the BR bands. In this time range, the B- and R-band fluxes have decreased by a factor of 0.57 and 0.77, respectively, with little B - R color change suggesting that the B and R bands luminosities change roughly like the bolometric luminosity. Hence, we multiplied the model value at 200 days by 0.67 (the mean of 0.57 and 0.77) to convert it to the value at 243 days. After the correction, the  $3\sigma$  stripped mass limit  $(M_{\rm st})$  for H $\alpha$  is  $<0.003\,M_{\odot}$ . For the other Balmer lines, the mass limits are also presented in

Table 7. For the He lines, their mass limits are obtained assuming that the luminosities of the He lines follow Equation (1) of Botyánszki et al. (2018).

For an He star companion, hydrogen lines would not be visible. Yet, a stripped mass of  $\lesssim 0.06\,M_\odot$  is expected, and the predicted strengths of the He lines are only a factor of a few smaller than the hydrogen lines in the H-rich companion star model (Botyánszki et al. 2018). No strong He emission lines in our data suggest a small amount of stripped He mass.

#### 4. Discussion

### 4.1. SD System as the Progenitor of SN 2021hpr

In Sections 3.3 and 3.4, we have shown that the companion interaction model can explain the early light excess and the color evolution of SN 2021hpr. The results suggest the possibility of an SD system with an  $\sim 9\,R_\odot$  companion star as the progenitor system of SN 2021hpr. An  $\sim 9\,R_\odot$  companion can be an SG star with  $6\,M_\odot$  or a low-mass RG (Hachisu et al. 1996). On the other hand, the radius of  $\sim 9\,R_\odot$  is too large for a low-mass MS star. An He-rich envelope star (He star) can also be a companion because its orbital separation a, assuming a circular orbit, ranges from 4 to  $80\,R_\odot$  (Hachisu et al. 1999) with  $a=2-3\,R_*$  for typical mass ratios (Hachisu et al. 1996; K10).

However, this interpretation needs to be reconciled with no signatures of  $H\alpha$  emission in the late spectrum, since we expect

 $<sup>\</sup>overline{^{23}}$  We adopted the form provided in Sand et al. (2018) as Equation (1) in Botyánszki et al. (2018).

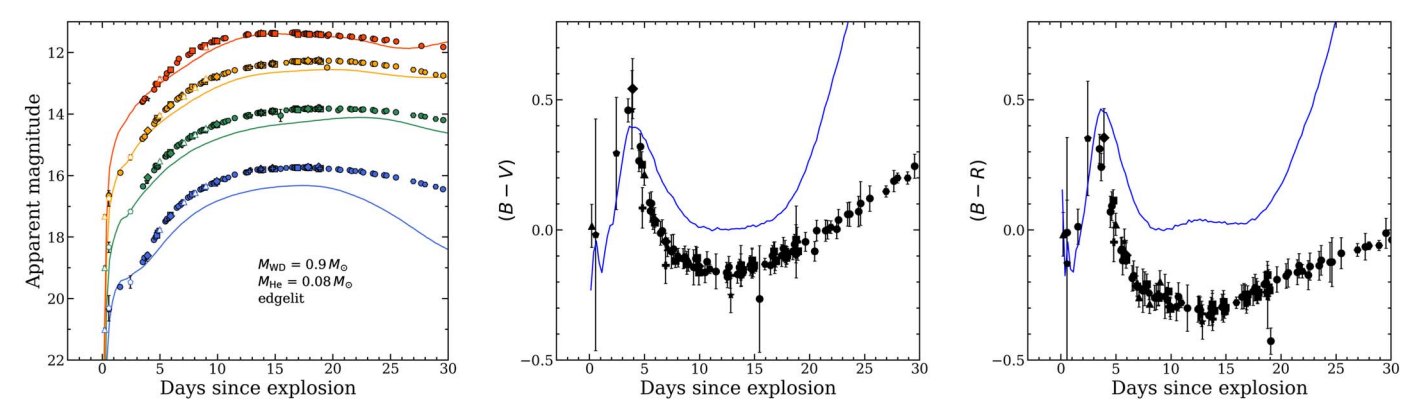


Figure 11. The light curve (left), B - V (middle), and B - R (right) color evolution of SN 2021hpr with the He shell (0.08  $M_{\odot}$ ) detonation on a 0.9  $M_{\odot}$  sub- $M_{\rm ch}$  mass WD (Polin et al. 2019). The color and symbols are the same as in Figure 2. In the color curves, the model is presented as the blue solid line.

to see strong nebular emission lines in a late phase for the SD model. We provide several possible ways to explain the nondetection of nebular lines.

Several works note that the stripped mass is reduced if the binary separation distance is large (Marietta et al. 2000; Pakmor et al. 2008; Liu et al. 2012; Pan et al. 2012; Boehner et al. 2017). Pakmor et al. (2008) demonstrates this in their Equation (4). Pakmor et al. (2008) show  $M_{\rm st} \sim a^{-3.5}$ . Applying this relation to their models, it is not too difficult to obtain the limit of  $M_{\rm st} < 0.01\,M_{\odot}$ . For example their rp3\_24a model, where the companion star's initial mass is 2.4  $M_{\odot}$  and the separation of the binary system is  $4.39 \times 10^{11}\,$  cm (or  $6.3\,R_{\odot}$ ), they get  $M_{\rm st} \sim 0.01\,M_{\odot}$ . Making a a bit larger will easily reduce  $M_{\rm st}$  to a value less than  $0.01\,M_{\odot}$ .

Pakmor et al. (2008) also showed that a low explosion energy produces a small amount of stripped mass (Equation (2) in Pakmor et al. 2008), so this could be another reason for the nondetection of H $\alpha$ . However, considering SN 2021hpr is a normal SN Ia event, a low explosion energy would make SN 2021hpr a subluminous event.

Overall, we conclude from the early multiband light curve that an SD binary system with a companion star with a stellar radius of  $\sim 9\,R_\odot$  can be the progenitor system of SN 2021hpr. However, no or weak nebular emission lines in a late phase pose a challenge to this interpretation. Further investigation on this issue is needed.

#### 4.2. DDet Model

As mentioned in the 1, the early color of SN 2021hpr can be regarded as a "red bump" in some DDet models. The DDet model is a model where a thermonuclear explosion in the He shell causes core ignition. DDet models with a thick He shell are known to produce excess in early light curves due to radioactive materials in He-shell ash (e.g., Polin et al. 2019). On the other hand, He-shell ash contains a large amount of Fegroup elements that block photons at short wavelengths and makes the SN color red. Qualitatively speaking, one would expect red excess light in the early light curve in thick He shell DDet models, which is possibly in agreement with SN 2021hpr's color and light curves.

Figure 11 compares the SN 2021hpr light and color curves with a thick He shell DDet model with a  $0.9\,M_\odot$  WD and a  $0.08\,M_\odot$  He shell (edge-lit) from Polin et al. (2019). The shape of the early red peak is similar to the observed colors but the model produces a slower evolution of the early red-band light curve than observed. Furthermore, the DDet model produces a

light curve that is too red at a later time (15 days since explosion in Figure 11). We conclude that DDet models have difficulties reproducing the SN 2021hpr light curve.

#### 4.3. Alternative Explosion Scenarios

Magee & Maguire (2020) demonstrate that early flux excess can be produced from the existence of a  $^{56}$ Ni clump, which depends on its mass, width, and location in the outer ejecta ( $^{56}$ Ni clump model). Figure 12 compares the light and color curves of SN 2021hpr with one of the  $^{56}$ Ni clump models (a  $0.005\,M_\odot$   $^{56}$ Ni clump with a width of  $0.06\,M_\odot$  superimposed on the fiducial light curve of SN 2018oh). This model is not completely consistent with the light curve of SN 2021hpr. Still, it produces the early red excess peak at  $B-V\sim0.5$  and keeps the color relatively blue at later epochs, but perhaps too blue, and qualitatively reproduces the observed light-curve features. Considering that the model does not require the production of H-Balmer emission lines in the nebular phase, it may provide a possible way to explain the early evolution of SN 2021hpr.

Levanon et al. (2015) derived an analytic form of an early signal emitted from the interaction between SN ejecta and DOM around the primary WD. This matter results from the tidal disruption of the companion WD. This emission is also expected to last up to a few hours at UV wavelengths. The light curves of SN 2012cg and iPTF2014atg were also examined for ejecta-DOM interaction in addition to other suggested models, such as a stratified <sup>56</sup>Ni structure, DDet with an outer <sup>56</sup>Ni shell, and companion interaction (Levanon & Soker 2017). In another study, Levanon & Soker (2019) argued that the early blue excess of SN 2018oh can be fitted with a two-component DOM interaction model better than a companion model. SN 2018oh is another SN without late-phase H $\alpha$  emission from stripped matter of its donor star in the SD system (Tucker et al. 2019), so the DOM model may be able to explain the observed properties of SN 2021hpr.

Wheeler (2012) pointed out that a strongly magnetized WD and an M dwarf star pair, which are quite common in the Galaxy, can be SN Ia progenitors. The material from the M dwarf star can be locked by their combined magnetic field ("magnetic bottle") on the magnetic pole of the WD, producing an SN Ia with an extra light source originating from material from the M dwarf and the accreted matter of the WD. It is not clear if SN 2021hpr can be explained with this model, but it will be interesting to investigate outcomes from this model further.

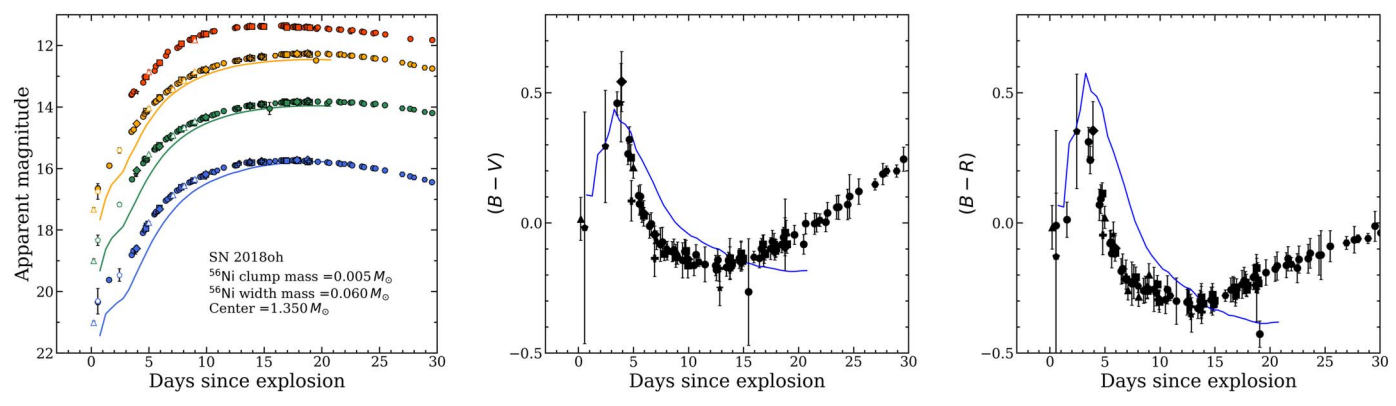
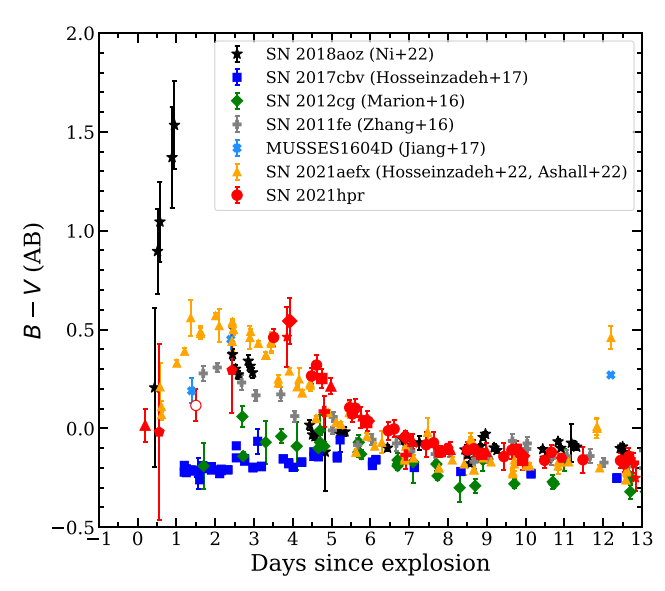


Figure 12. Same as Figure 11 but with a  $^{56}$ Ni clump of  $0.005 M_{\odot}$  and with a width of  $0.06 M_{\odot}$  located on the mass coordinate of  $1.35 M_{\odot}$  based on the fiducial light curve of SN 2018oh (Magee & Maguire 2020).



**Figure 13.** The dereddened B-V color evolution of SN 2021hpr with other SNe Ia within 13 days since the explosion. A data point for SN 2021hpr is added with a red open circle at  $t \sim 1.5$  days by converting B-R to B-V using a correlation between the two quantities during the first four days since the explosion. For SN 2021aefx, we plotted both photometry in Ashall et al. (2022), including ground and Swift data, and Hosseinzadeh et al. (2022). Since there was no estimated explosion time in Hosseinzadeh et al. (2022), we use the explosion time (59529.19 MJD) in Ashall et al. (2022). The SNe Ia, except SN 2011fe, are known to have early an excess. The symbols of SN 2021hpr are the same as in Figure 2.

#### 4.4. Comparison of Color Curves with Other SNe Ia

In Figure 13, we compare early color curves of several SNe Ia with an extensive set of early-time data, five with early excess (SN 2012cg, MUSSES1604D, SN 2017cbv, SN 2018aoz, and SN 2021aefx) and one without early excess (SN 2011fe). Figure 13 reveals a diversity of early color curves. The figure indicates that there are roughly four families of color curves, one with a blue, flat color curve (SN 2017cbv and SN 2012cg), one with a red peak at 2–3 days, and then either becoming redder again (MUSSES1604D) or blue (SN 2021hpr, SN 2011fe, and SN 2021aefx), and one that shows a red peak at a very early epoch (~1 day) and becomes blue (SN 2018aoz). These different behaviors may reflect the differences in the explosion mechanisms.

For the first category of flat, blue curves of SN 2017cbv and SN 2012cg, Hosseinzadeh et al. (2017) suggest a model with

CSM material and nickel mixing. They disfavor the companion interaction model because such a model cannot explain the excess in the Swift UV bands. It will also difficult to keep the color curve blue in the early epoch with an SD model which predicts an early red peak as in Figure 6.

In the second category of SNe with an early red peak and a subsequent reddening, MUSSES1604D follows the DDet model trend well, where its red color can be explained by the presence of Fe-peak elements in the outer layer ejecta extinguishing blue light. The outer layer ejecta are possibly produced by He-shell burning in DDet models (Jiang et al. 2017).

For the third category of SNe with an early red peak, followed by a blue light curve, SHCE can explain the observed properties as found for SN 2021hpr. Similarly, the B-V color of SN 2021aefx reaches a peak ( $\sim$ 0.6) at  $\sim$ 2 days, a bit faster than that of SN 2021hpr. Like SN 2021hpr, the early flux and color evolution of SN 2021aefx can be explained at least partly by companion interaction (Hosseinzadeh et al. 2022). However, there is no perfect explanation for all of the observed properties of SN 2021aefx for now despite many efforts in terms of the progenitor scenarios (Hosseinzadeh et al. 2022). On the other hand, the work of Ashall et al. (2022) cautions that the early UV emission excess of SN 2021aefx can be affected by the Doppler effect and the interpretation of the excess needs to take into account such effects. The lack of early excess emission for SN 2011fe may be due to a less optimal viewing angle suppressing the early excess emission or a very small companion star, although other possibilities (DDet models with thin He shells) can be considered.

For the last category of a very early red peak of SN 2018aoz, the companion shock-heating model is disfavored since such a model cannot reproduce the color curve behavior. The color behavior can be explained by an overabundance of Fe-peak elements due to burning in the extreme outer layer, such as those in DDet models (Ni et al. 2022). Also, Ni et al. (2022) suggest the possibility of extended subsonic mixing to explain the presence of outer layer Fe-peak elements.

The light curves of SNe Ia can look alike and be parameterized as a uniform population, but a closer look at the early colors curves shows a wide variety of cases. This can be due to a variety of explosion mechanisms taking place. Hence, it is highly desirable to expand the SN Ia sample with very early multiband light curves to make a more statistically meaningful study.

#### 5. Summary

We observed an SN Ia, SN 2021hpr, first reported on 2021 April 2.45 UT, using our IMSNG network of 0.4–1.0 m class telescopes. A long-term light curve and a series of long-slit spectra show that SN 2021hpr is close to a normal SN Ia with a distance modulus of  $33.28 \pm 0.11$  mag  $(d=45.23 \pm 2.31 \, \mathrm{Mpc})$ .

Our analysis of the early photometric data reveals the distinct feature of SHCE. We fit the early data using a two-component model made of an ejecta–companion interaction component and a simple power-law component. The model explains the early excess in the light curve and color evolution. With the assumption of the optimal viewing angle, the best-fit result is consistent with a companion radius of  $8.84 \pm 0.58\,R_\odot$ . The radius could be larger if the viewing angle is different. An SG star, a low-mass RG, or a helium star can be a possible donor but a low-mass MS star is not likely to be the progenitor companion. We could not detect a probable progenitor candidate of SN 2021hpr in deep, preexplosion, archival HST images. The multiband HST detection limits rule out massive stars with  $M_{\rm init} > 10\,M_\odot$  as the progenitor, giving us an upper limit on the radius of the progenitor system of  $\sim 215\,R_\odot$ .

Although the SD companion model can explain the early multiband light-curve evolution of SN 2021hpr, we could not find any strong signature of stripped mass ( $\lesssim 0.003\,M_\odot$  for  ${\rm H}\alpha$  emission) of H/He-rich material from the companion star in the late spectroscopy. This can result from a large binary separation rather than a low SN explosion energy, but the nondetection of the nebular lines needs further theoretical and observational investigation. In particular, we did not analyze the early evolution of SN 2021hpr using DDet or DOM models in detail. Future, careful investigation may find that these two models can explain this distinct SN.

To understand the SN Ia explosion mechanism, we compared color curves of SNe Ia with available very early B - V data (available at <1–2 days). These color curves have a diversity that can be summarized into four cases: (i) a color curve showing a very early red peak (\$\leq 1\) day after explosion) like SN 2018aoz; (ii) color curves with a slower appearance of a red peak (2-3 days after explosion), with reddening of the curve in a later time (MUSSES1604D); (iii) or with the color staying blue after the red peak (SN 2021hpr, SN 2011fe, and SN 2021aefx); and (iv) flat, blue color curve (SN 2017cbv). The first two cases support He-shell detonation or at least <sup>56</sup>Ni in the outer ejecta, but a simple comparison with DDet models does not reproduce the early light and color curves of SN 2021hpr. A companion interaction model can explain the light and color curves of SN 2021hpr well, making this SN distinct from SNe Ia like SN 2018aoz (very early red peak), SN 2017cbv (flat blue color curve), and MUSSES1604D (slow red peak, late red color). Different early color properties of various SNe Ia suggest that the SN Ia explosion mechanism is diverse.

The excellent agreement between the observed multiband light curves and the SHCE model with an SD progenitor system is tantalizing but enigmatic, with the nondetection of nebular lines at late phases. An enlarged sample of SNe Ia with data of this kind and an extensive study of light curves should tell us how diverse the SN Ia explosion mechanism can be. Also, the detection of the early excess of SN 2021hpr demonstrates that high-cadence monitoring of nearby galaxies using small telescopes is a powerful tool to constrain the

progenitor system of SN Ia even in the the era of large telescopes.

This work was supported by the National Research Foundation of Korea (NRF) grants, No. 2020R1A2C3011091 and No. 2021M3F7A1084525, funded by the Korea government, and the Korea Astronomy and Space Science Institute under the R&D program (Project No. 2022-1-860-03) supervised by the Ministry of Science and ICT (MSIT). G.L. acknowledges support from the Basic Science Research Program through NRF funded by MSIT (No. 2021 R1A6A3A13045313) and MSIT (No. 2022R1A6A3A 01085930). S.C.Y. is supported by the NRF grant (NRF-2019R1A2C2010885). J.C.W. and B.P.T. are also supported by a DOE grant to the Wooten Center for Astrophysical Plasma Properties (WCAPP; PI Don Winget). J.V. is also supported by the project "Transient Astrophysical Objects" GINOP 2.3.2-15-2016-00033 of the National Research, Development and Innovation Office (NKFIH), Hungary, funded by the European Union. D.K. acknowledges support by the NRF of Korea (NRF) grant (No. 2021R1C1C1013580) funded by MSIT.

The Hobby–Eberly Telescope (HET) is a joint project of the University of Texas at Austin, the Pennsylvania State University, Ludwig-Maximilians-Universität München, and Georg-August-Universität Göttingen. The HET is named in honor of its principal benefactors, William P. Hobby and Robert E. Eberly.

The Low Resolution Spectrograph 2 (LRS2) was developed and funded by the University of Texas at Austin McDonald Observatory and Department of Astronomy and by Pennsylvania State University. We thank the Leibniz-Institut für Astrophysik Potsdam (AIP) and the Institut für Astrophysik Göttingen (IAG) for their contributions to the construction of the integral field units.

We acknowledge the Texas Advanced Computing Center (TACC) at The University of Texas at Austin for providing high performance computing, visualization, and storage resources that have contributed to the results reported within this paper.

We thank the staff at the SAO, MAO, CBNUO, LOAO, SOAO, DOAO, and McDonald Observatories for their observations and maintenance of the facilities. This research made use of the data taken with LOAO and SOAO are operated by the Korea Astronomy and Space Science Institute (KASI), DOAO of National Youth Space Center (NYSC), HET of McDonald Observatory, and CBNUO of Chungbuk National University Observatory.

Facilities: LOAO, SOAO, DOAO, MAO: 1.5 m; SAO, CBNUO: 0.6 m; McDonald Observatory: HET, HST.

Software: Python packages: Astropy (Astropy Collaboration et al. 2013), Numpy (Harris et al. 2020), LMFIT (Newville et al. 2014), PyRAF (Science Software Branch at STScI 2012), Hotpants (Becker 2015), Astronometry.net (Lang et al. 2010), SExtractor (Bertin & Arnouts 1996), and AstroDrizzle (Gonzaga et al. 2012).

#### Appendix Figures

Figure A1 shows the light and color curves that correspond to the common viewing angle and other variant DDC models from Blondin et al. (2013) and Dessart et al. (2014).

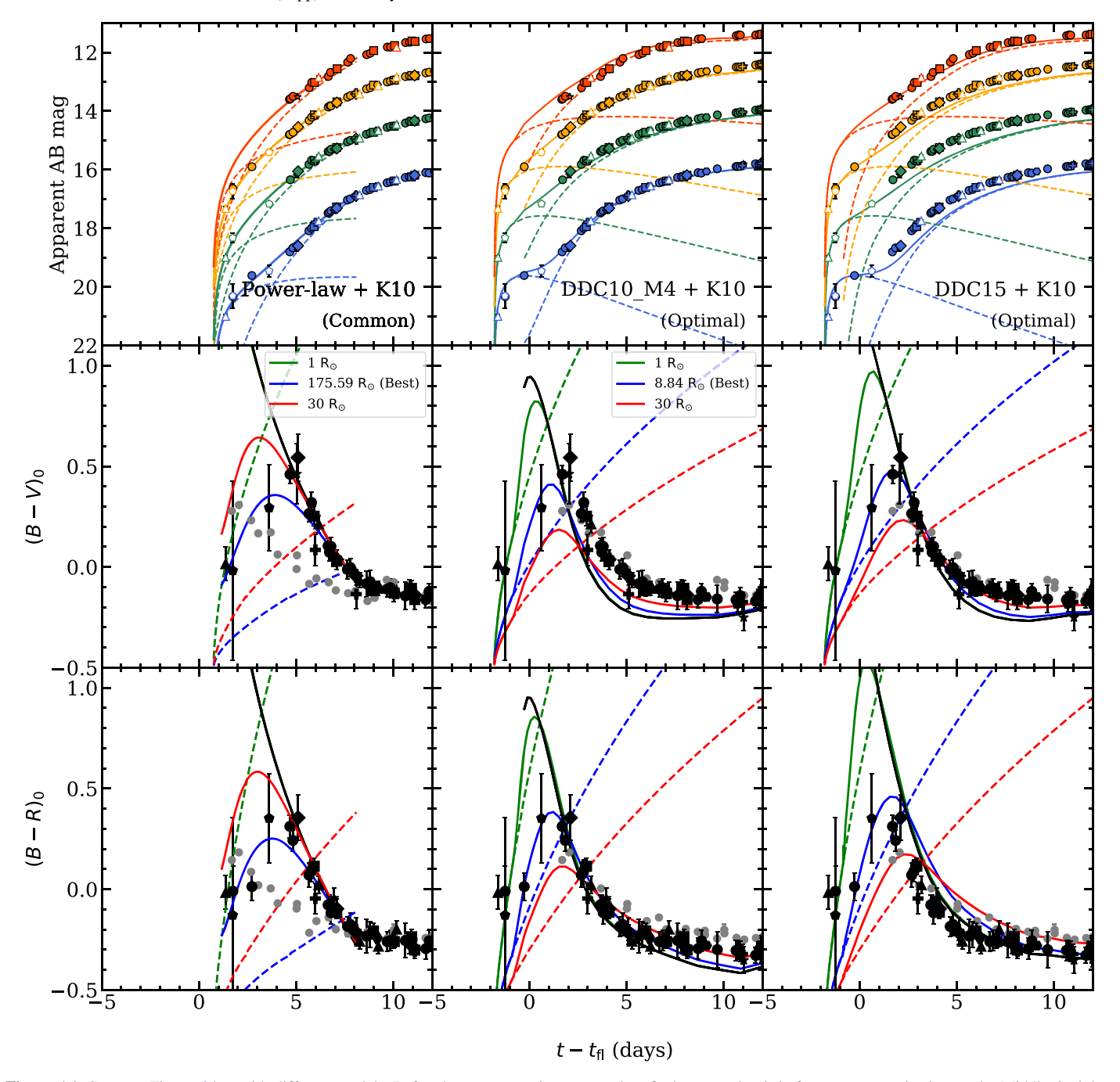


Figure A1. Same as Figure 6 but with different models. Left column: companion+power-law fit, but note that it is for a common viewing angle. Middle & right columns: cases for the optimal viewing angle using DDC10\_M4 (middle) and DDC15 model (right) with the best-fit SHCE model from Figure 6.

#### **ORCID iDs**

Gu Lim https://orcid.org/0000-0002-5760-8186
Myungshin Im https://orcid.org/0000-0002-8537-6714
Gregory S. H. Paek https://orcid.org/0000-0002-6639-6533
Sung-Chul Yoon https://orcid.org/0000-0002-5847-8096
Changsu Choi https://orcid.org/0000-0001-8642-1241
Sophia Kim https://orcid.org/0000-0002-0070-1582
J. Craig Wheeler https://orcid.org/0000-0003-1349-6538
Benjamin P. Thomas https://orcid.org/0000-0002-0977-1974

Jozsef Vinkó https://orcid.org/0000-0001-8764-7832 Dohyeong Kim https://orcid.org/0000-0002-6925-4821 Wonseok Kang https://orcid.org/0000-0003-3390-1924

Taewoo Kim https://orcid.org/0000-0003-4686-5109 Hyun-Il Sung https://orcid.org/0000-0001-9515-3584 Shuhrat Ehgamberdiev https://orcid.org/0000-0001-9730-3769

Otabek Burhonov https://orcid.org/0000-0003-1169-6763 Davron Mirzaqulov https://orcid.org/0000-0003-0570-6531

#### References

Amanullah, R., Lidman, C., Rubin, D., et al. 2010, ApJ, 716, 712
Ashall, C., Lu, J., Shappee, B. J., et al. 2022, ApJL, 932, L2
Astropy Collaboration, Robitaille, T. P., Tollerud, E. J., et al. 2013, A&A, 558, A33

```
Becker, A. 2015, HOTPANTS: High Order Transform of PSF ANd Template
   Subtraction, Astrophysics Source Code Library, ascl:1504.004
Bellm, E. C., Kulkarni, S. R., Graham, M. J., et al. 2019, PASP, 131, 018002
Bertin, E. 2010, SWarp: Resampling and Co-adding FITS Images Together,
   Astrophysics Source Code Library, ascl:1010.068
Bertin, E., & Arnouts, S. 1996, A&AS, 117, 393
Biscardi, I., Brocato, E., Arkharov, A., et al. 2012, A&A, 537, A57
Blanton, M. R., & Roweis, S. 2007, AJ, 133, 734
Blondin, S., Dessart, L., Hillier, D. J., et al. 2013, MNRAS, 429, 2127
Bloom, J. S., Kasen, D., Shen, K. J., et al. 2012, ApJL, 744, L17
Boehner, P., Plewa, T., & Langer, N. 2017, MNRAS, 465, 2060
Bottinelli, L., Gouguenheim, L., Paturel, G., et al. 1984, A&AS, 56, 381
Bottinelli, L., Gouguenheim, L., Paturel, G., et al. 1986, A&A, 156, 157
Botyánszki, J., Kasen, D., & Plewa, T. 2018, ApJL, 852, L6
Cao, Y., Kulkarni, S. R., Howell, D. A., et al. 2015, Natur, 521, 328
Choi, J., Dotter, A., Conroy, C., et al. 2016, ApJ, 823, 102
Chonis, T. S., Hill, G. J., Lee, H., et al. 2014, Proc. SPIE, 9147, 91470A
Chugai, N. N. 1986, SvA, 30, 563
Contreras, C., Phillips, M. M., Burns, C. R., et al. 2018, ApJ, 859, 24
Dessart, L., Blondin, S., Hillier, D. J., et al. 2014, MNRAS, 441, 532
Ehgamberdiev, S. 2018, NatAs, 2, 349
Fink, M., Hillebrandt, W., & Röpke, F. K. 2007, A&A, 476, 1133
Fink, M., Röpke, F. K., Hillebrandt, W., et al. 2010, A&A, 514, A53
Fitzpatrick, E. L. 1999, PASP, 111, 63
Gonzaga, S., Hack, W., Fruchter, A., et al. 2012, The DrizzlePac Handbook,
   HST Data Handbook (Baltimore, MD: STScI)
Groenewegen, M. A. T., & Sloan, G. C. 2018, A&A, 609, A114
Hachisu, I., Kato, M., & Nomoto, K. 1996, ApJL, 470, L97
Hachisu, I., Kato, M., Nomoto, K., et al. 1999, ApJ, 519, 314
Han, X., Zheng, W., Stahl, B. E., et al. 2020, ApJ, 892, 142
Harris, C. R., Millman, K. J., van der Walt, S. J., et al. 2020, Natur, 585, 357
Harutyunyan, A. H., Pfahler, P., Pastorello, A., et al. 2008, A&A, 488, 383
Hicken, M., Challis, P., Jha, S., et al. 2009, ApJ, 700, 331
Hosseinzadeh, G., Sand, D. J., Lundqvist, P., et al. 2022, ApJL, 933, L45
Hosseinzadeh, G., Sand, D. J., Valenti, S., et al. 2017, ApJL, 845, L11
Iben, I., & Tutukov, A. V. 1984, ApJS, 54, 335
Im, M., Choi, C., Hwang, S., et al. 2019, JKAS, 52, 11
Im, M., Choi, C., Yoon, S.-C., et al. 2015, ApJS, 221, 22
Im, M., Kim, Y., Lee, C.-U., et al. 2021, JKAS, 54, 89
Im, M., Ko, J., Cho, Y., et al. 2010, JKAS, 43, 75
Itagaki, K. 2021, TNSTR, 2021-998
Jeon, Y., Im, M., Ibrahimov, M., et al. 2010, ApJS, 190, 166
Jha, S., Riess, A. G., & Kirshner, R. P. 2007, ApJ, 659, 122
Jiang, J.-A., Doi, M., Maeda, K., et al. 2017, Natur, 550, 80
Kasen, D. 2010, ApJ, 708, 1025
Kawabata, M., Maeda, K., Yamanaka, M., et al. 2020, ApJ, 893, 143
Khokhlov, A. M. 1991, A&A, 245, 114
Kowalski, M., Rubin, D., Aldering, G., et al. 2008, ApJ, 686, 749
Lang, D., Hogg, D. W., Mierle, K., et al. 2010, AJ, 139, 1782
Leonard, D. C. 2007, ApJ, 670, 1275
Levanon, N., & Soker, N. 2017, MNRAS, 470, 2510
Levanon, N., & Soker, N. 2019, ApJL, 872, L7
Levanon, N., Soker, N., & García-Berro, E. 2015, MNRAS, 447, 2803
Levesque, E. M., Massey, P., Olsen, K. A. G., et al. 2005, ApJ, 628, 973
Li, L., Zhang, J., Dai, B., et al. 2022, ApJ, 924, 35
Li, W., Bloom, J. S., Podsiadlowski, P., et al. 2011, Natur, 480, 348
Li, W., Wang, X., Vinkó, J., et al. 2019, ApJ, 870, 12
Liu, Z. W., Pakmor, R., Röpke, F. K., et al. 2012, A&A, 548, A2
Liu, Z.-W., & Stancliffe, R. J. 2016, MNRAS, 459, 1781
Lundqvist, P., Nyholm, A., Taddia, F., et al. 2015, A&A, 577, A39
Magee, M. R., & Maguire, K. 2020, A&A, 642, A189
Magnier, E. A., Schlafly, E., Finkbeiner, D., et al. 2013, ApJS, 205, 20
```

```
Maguire, K., Taubenberger, S., Sullivan, M., et al. 2016, MNRAS, 457, 3254
Marietta, E., Burrows, A., & Fryxell, B. 2000, ApJS, 128, 615
Marion, G. H., Brown, P. J., Vinkó, J., et al. 2016, ApJ, 820, 92
Mazzali, P. A., Sullivan, M., Hachinger, S., et al. 2014, MNRAS, 439, 1959
McCully, C., Jha, S. W., Foley, R. J., et al. 2014, Natur, 512, 54
Medford, M. S., Lu, J. R., & Schlafly, E. F. 2020, RNAAS, 4, 38
Meng, X., Chen, X., & Han, Z. 2007, PASJ, 59, 835
Newville, M., Stensitzki, T., Allen, D. B., et al. 2014, LMFIT: Non-Linear
  Least-Square Minimization and Curve-Fitting for Python, v0.8.0, Zenodo,
  doi:10.5281/zenodo.11813
Ni, Y. Q., Moon, D.-S., Drout, M. R., et al. 2022, NatAs, 6, 568
Noebauer, U. M., Kromer, M., Taubenberger, S., et al. 2017, MNRAS,
Nomoto, K. 1982, ApJ, 253, 798
Nugent, P. E., Sullivan, M., Cenko, S. B., et al. 2011, Natur, 480, 344
Pakmor, R., Kromer, M., Taubenberger, S., et al. 2013, ApJL, 770, L8
Pakmor, R., Röpke, F. K., Weiss, A., et al. 2008, A&A, 489, 943
Pan, K.-C., Ricker, P. M., & Taam, R. E. 2012, ApJ, 750, 151
Parodi, B. R., Saha, A., Sandage, A., et al. 2000, ApJ, 540, 634
Pereira, R., Thomas, R. C., Aldering, G., et al. 2013, A&A, 554, A27
Perlmutter, S., Aldering, G., Goldhaber, G., et al. 1999, ApJ, 517, 565
Phillips, M. M. 1993, ApJL, 413, L105
Phillips, M. M., Lira, P., Suntzeff, N. B., et al. 1999, AJ, 118, 1766
Piro, A. L., & Morozova, V. S. 2016, ApJ, 826, 96
Piro, A. L., & Nakar, E. 2013, ApJ, 769, 67
Planck Collaboration, Ade, P. A. R., Aghanim, N., et al. 2016, A&A, 594, A13
Polin, A., Nugent, P., & Kasen, D. 2019, ApJ, 873, 84
Press, W. H., Teukolsky, S. A., Vetterling, W. T., et al. 1992(2nd ed.;
  Cambridge: Univ. Press)
Prieto, J. L., Rest, A., & Suntzeff, N. B. 2006, ApJ, 647, 501
Rabinak, I., & Waxman, E. 2011, ApJ, 728, 63
Reindl, B., Tammann, G. A., Sandage, A., et al. 2005, ApJ, 624, 532
Riess, A. G., Filippenko, A. V., Challis, P., et al. 1998, AJ, 116, 1009
Sand, D. J., Graham, M. L., Botyánszki, J., et al. 2018, ApJ, 863, 24
Schlafly, E. F., & Finkbeiner, D. P. 2011, ApJ, 737, 103
Science Software Branch at STScI 2012, Astrophysics Source Code Library,
  ascl:1207.011
Shappee, B. J., Piro, A. L., Stanek, K. Z., et al. 2018, ApJ, 855, 6
Smitka, M. T., Brown, P. J., Suntzeff, N. B., et al. 2015, ApJ, 813, 30
Takanashi, N., Doi, M., & Yasuda, N. 2008, MNRAS, 389, 1577
Tomasella, L., Benetti, S., Cappellaro, E., et al. 2021, TNSCR, 2021-1031
Tonry, J. L., Stubbs, C. W., Lykke, K. R., et al. 2012, ApJ, 750, 99
Tsvetkov, D. Y., Pavlyuk, N. N., Ikonnikova, N. P., et al. 2021, ATel,
  14541, 1
Tucker, M. A., Shappee, B. J., & Wisniewski, J. P. 2019, ApJL, 872, L22
Tully, R. B., Courtois, H. M., Dolphin, A. E., et al. 2013, AJ, 146, 86
Tully, R. B., & Fisher, J. R. 1988, in Catalog of Nearby Galaxies, ed.
  R. B. Tully & J. R. Fisher (Cambridge, UK: Cambridge Univ. Press), 224
Wang, B., Meng, X., Liu, D.-D., et al. 2014, ApJL, 794, L28
Wang, X., Wang, L., Pain, R., et al. 2006, ApJ, 645, 488
Ward, S. M., Thorp, S., Mandel, K. S., et al. 2022, arXiv:2209.10558
Webbink, R. F. 1984, ApJ, 277, 355
Wheeler, J. C. 2012, ApJ, 758, 123
Wheeler, J. C., Lecar, M., & McKee, C. F. 1975, ApJ, 200, 145
Whelan, J., & Iben, I. 1973, ApJ, 186, 1007
Woosley, S. E., Taam, R. E., & Weaver, T. A. 1986, ApJ, 301, 601
Yamanaka, M., Maeda, K., Kawabata, M., et al. 2014, ApJL, 782, L35
Yaron, O. 2019, TNSAN, 2019-60
Zhang, J.-J., Wang, X.-F., Bai, J.-M., et al. 2014, AJ, 148, 1
Zhang, K., Wang, X., Zhang, J., et al. 2016, ApJ, 820, 67
Zhang, Y., Zhang, T., Danzengluobu, et al. 2022, PASP, 134, 074201
Zheng, W., Silverman, J. M., Filippenko, A. V., et al. 2013, ApJL, 778, L15
```